Cell Stem Cell

A human pluripotent stem cell-based somitogenesis model using microfluidics

--Manuscript Draft--

Manuscript Number:	CELL-STEM-CELL-D-23-00588R3
Full Title:	A human pluripotent stem cell-based somitogenesis model using microfluidics
Article Type:	Research Article
Keywords:	human pluripotent stem cell; somite formation; in vitro modeling; microfluidics; biomechanics
Corresponding Author:	Jianping Fu, Ph.D. University of Michigan Ann Arbor, MI UNITED STATES
First Author:	Yue Liu
Order of Authors:	Yue Liu
	Yung Su Kim
	Xufeng Xue
	Yuchuan Miao
	Norio Kobayashi
	Shiyu Sun
	Robin Zhexuan Yan
	Qiong Yang
	Olivier Pourquié
	Jianping Fu, Ph.D.
Abstract:	Emerging human pluripotent stem cell (hPSC)-based embryo models are useful for studying human embryogenesis. Particularly, there are hPSC-based somitogenesis models using free-floating culture that recapitulate somite formation. Somitogenesis in vivo involves intricately orchestrated bio-chemical and -mechanical events. However, none of the current somitogenesis models controls biochemical gradients or biomechanical signals in the culture, limiting their applicability to untangle complex biochemical-biomechanical interactions that drive somitogenesis. Here we report a new human somitogenesis model by confining hPSC-derived presomitic mesoderm (PSM) tissues in microfabricated trenches. Exogenous microfluidic morphogen gradients imposed on PSM cause axial patterning and trigger spontaneous rostral-to-caudal somite formation. A mechanical theory is developed to explain the size dependency between somites and PSM. The microfluidic somitogenesis model is further exploited to reveal regulatory roles of cellular and tissue biomechanics in somite formation. This study presents a useful microengineered, hPSC-based model for understanding the bio-chemical and -mechanical events that guide somite formation.
Additional Information:	
Question	**Response**
Original Code Does this manuscript report original code?	No
Standardized datasets Does this manuscript report new standardized datasets? A list of datatypes considered standardized under Cell Press	Yes

policy is available here. This includes next-generation sequencing, microarray, proteomics, and metabolomics datasets. Please note that the editors at Cell Stem Cell will NOT send the paper for in depth review if access to standardized datasets is not provided to Reviewers.	
Reviewers must have anonymous access to these standardized datasets that is free-of-cost. Please provide dataset locations and instructions for access here. If applicable, include accession numbers and reviewer tokens. Please consult these Author's guides for more information: "Standardized datatypes, datatype-specific repositories, and general-purpose repositories recommended by Cell Press" and "How standardized datasets and original code accompany Cell Press manuscripts from submission through publication" or email us at stemcell@cell.com. as follow-up to "**Standardized datasets** Does this manuscript report new standardized datasets? A list of datatypes considered standardized under Cell Press policy is available here. This includes next-generation sequencing, microarray, proteomics, and metabolomics datasets. Please note that the editors at Cell Stem Cell will NOT send the paper for in depth review if access to standardized datasets is not provided to Reviewers. "	The scRNA-seq data supporting this study's results are deposited at Gene Expression Omnibus with accession number GSE236668.
Original code<p> Does this manuscript report original computer code, algorithms, or computational models?	No
Standardized datasets<p>A list of datatypes considered standardized under Cell Press policy is available here. Does this manuscript report new standardized datasets?	Yes
Reviewers must have free and anonymous access to these standardized	ScRNA-seq data supporting this study's results are deposited at Gene Expression Omnibus with accession number GSE236668. Entries from Supplementary Tables S1

datasets. Please provide dataset locations and instructions for access here. If applicable, include accession numbers and reviewer tokens. If you don't specify access information, your manuscript will not be sent to reviewers.<p>Please consult these guides for more information: “Standardized datatypes, datatype-specific repositories, and general-purpose repositories recommended by Cell Press" and “How standardized datasets and original code accompany Cell Press manuscripts from submission through publication.” Email us at stemcell@cell.com if you have any questions. as follow-up to "Standardized datasets<p>A list of datatypes considered standardized under Cell Press policy is available here. Does this manuscript report new standardized datasets?"	& S2 were deposited on Mendeley at 10.17632/z4jncwx9ks.1.

Cover Letter

Jianping Fu, Ph.D.
Professor
Mechanical Engineering
Biomedical Engineering
Cell & Developmental Biology

2664 G.G. Brown Addition
2350 Hayward Street
Ann Arbor, MI 48109-2125

Office. (734) 615-7363
Mobile. (734) 369-0116
Fax. (734) 647-9379
jpfu@umich.edu
http://me.engin.umich.edu/ibbl

5/29/2024

Dear Dr. Weber,

Thank you for editing our manuscript, entitled "A human pluripotent stem cell-based somitogenesis model using microfluidics", that was submitted to *Cell Stem Cell*. In the latest version, we have revised the supplemental video titles, the data and code availability statement, and the key resource table. Notably, we uploaded an extra supplemental table (Table S3) to Mendeley, which contains all the oligonucleotides used in this study. The updated data are still pending for approval on Mendeley at the time of this submission but are expected to be publicly available before the publication of our manuscript.

On behalf of my fellow co- authors, I appreciate your efforts in this work.

Sincerely,

Jianping Fu, Ph.D.

Reviewer #1: The authors have addressed all of our initial comments, and we are pleased to recommend that the paper be accepted.

Reviewer #3: The authors addressed most of my critiques. I don't see the point of raising new questions or detailly discussing some of the unresolved issues. In short, I support the publication of this beautiful work in its current form. Ertugrul Ozbudak.

We would like to express our gratitude to the reviewers for their dedicated efforts in evaluating our manuscript. Their thoughtful critiques and constructive suggestions have played a pivotal role in enhancing the overall quality of our work. We appreciate the time and expertise each reviewer has contributed, collectively making a substantial impact on the improvement of our manuscript and are glad to see that the reviewers are satisfied with the revision.

A human pluripotent stem cell-based somitogenesis model using microfluidics

Yue Liu[1] *, Yung Su Kim[1], Xufeng Xue[1], Yuchuan Miao[4, 5], Norio Kobayashi[1], Shiyu Sun[1], Robin Zhexuan Yan[1], Qiong Yang[2, 3], Olivier Pourquié[4, 5, 6], and Jianping Fu[1, 7, 8] *

[1]Department of Mechanical Engineering, University of Michigan, Ann Arbor, Michigan 48109, USA; [2]Department of Biophysics, University of Michigan, Ann Arbor, Michigan 48109, USA; [3]Department of Physics, University of Michigan, Ann Arbor, Michigan 48109, USA; [4]Department of Genetics, Harvard Medical School, Boston, Massachusetts 02115, USA; [5]Department of Pathology, Brigham and Women's Hospital, Boston, Massachusetts 02115, USA; [6]Harvard Stem Cell Institute, Harvard University, Cambridge, Massachusetts 02138, USA; [7]Department of Biomedical Engineering, University of Michigan, Ann Arbor, Michigan 48109, USA; [8]Department of Cell & Developmental Biology, University of Michigan Medical School, Ann Arbor, MI 48109, USA.

*Correspondence and requests for materials should be addressed to Y.L. (email: umliu@umich.edu) or J.F. (lead contact, email: jpfu@umich.edu)

SUMMARY

Emerging human pluripotent stem cell (hPSC)-based embryo models are useful for studying human embryogenesis. Particularly, there are hPSC-based somitogenesis models using free-floating culture that recapitulate somite formation. Somitogenesis *in vivo* involves intricately orchestrated biochemical and biomechanical events. However, none of the current somitogenesis models controls biochemical gradients or biomechanical signals in the culture, limiting their applicability to untangle complex biochemical-biomechanical interactions that drive somitogenesis. Here, we develop a human somitogenesis model by confining hPSC-derived presomitic mesoderm (PSM) tissues in microfabricated trenches. Exogenous microfluidic morphogen gradients imposed on PSM cause axial patterning and trigger spontaneous rostral-to-caudal somite formation. A mechanical theory is developed to explain the size dependency between somites and PSM. The microfluidic somitogenesis model is further exploited to reveal regulatory roles of cellular and tissue biomechanics in somite formation. This study presents a useful microengineered, hPSC-based model for understanding the biochemical and biomechanical events that guide somite formation.

INTRODUCTION

The formation of morphological boundaries between developing tissues is an integral mechanism for generating body forms and functions. In particular, formation of somites dictates the body layout of a vertebrate embryo and ultimately the structure of its musculoskeletal system. During somitogenesis, the presomitic mesoderm (PSM), a bilateral strip of mesenchymal tissue flanking the forming neural tube, progressively segments into bilaterally symmetrical epithelial somites in a rostral (R)-to-caudal (C) direction (**Figure 1a**). New somites are formed at the rostral end of the PSM, where cells undergo mesenchymal-epithelial transition (MET) and coalesce into a rosette-like structure that pulls apart from the PSM. Although theories have been proposed to correlate somitogenesis dynamics with biochemical signals such as antiparallel gradients of FGF / WNT / retinoic acid (RA) along the R-C axis in the PSM[1-4], detailed mechanisms underlying somitogenesis remain elusive owing to the inaccessibility of *in vivo* models for modulating endogenous morphogen gradients, especially for mammalian species. Particularly, the segmentation of somite, in which nascent somite delaminates from the PSM tissue, involves a mechanical process of boundary establishment and incites intriguing analogy with fracture in solids and Rayleigh-Plateau instability in fluids[5]. Recent studies of biochemical dynamics within the PSM provide critical insights towards how the fate of presumptive somitic cells is specified by the spatiotemporal interaction between segmentation clock and Fgf/ppErk signaling[4,6]. Nonetheless, a full account for mechanical driving forces responsible the ultimate mechanical delamination of nascent somites from the rostral PSM following somitic lineage fate specification remains a key component that needs to be fully elucidated for understanding the somite size and number regulation.

The recent emergence of hPSC-based embryo models opens up exciting opportunities to promote fundamental understanding of human development[7-9]. Particularly, there are hPSC-based somitogenesis models recently developed based on three-dimensional, free-floating cultures that show somite formation[10-14]. However, none of the models controls biochemical gradients or biomechanical signals in the culture, limiting their applicability to untangle complex biochemical-biomechanical interactions that drive somitogenesis. In this work we develop a human somite formation model by mechanically confining hPSC-derived PSM tissues in microfabricated trenches to simulate an essential mechanical boundary condition for PSM development *in vivo*[15,16]. Controlled exogenous microfluidic morphogen gradients are then

imposed on the PSM tissues to drive their R-C patterning and trigger spontaneous somite formation, beginning rostrally and extending caudally. Leveraging the compatibility of this human somite formation model with live imaging and biomechanical and molecular characterizations and perturbations, we further experimentally and theoretically explored the mechanical regulators that contribute to somite formation and size regulation.

RESULTS

A hPSC-based, microfluidic somite development model

To model the sculpting of somites, we developed a hPSC-based, microfluidic somite development model (μSDM). Specifically, μSDM develops in a polydimethylsiloxane (PDMS)-based microfluidic device containing three channels partitioned by circular support posts (see **Methods** for μSDM design considerations; **Figure S1a&b**). Rectangular micro-trench structures (width: 200 μm; length: 4 mm; depth: 200 μm) at the bottom surface of the central channel of the microfluidic device are used to position and contain hPSC-derived PSM tissues, to mimic their geometrical confinements and mechanical boundary condition *in vivo*[15,16] (see **Methods**). With different signaling molecules supplemented to the two reservoirs of the central channel, gradients of developmental signals, such as RA, FGF and WNT, could be explicitly imposed on PSM cells seeded in micro-trenches through passive diffusion (**Figure S1a&c**). Indeed, passive diffusion assays using fluorescent dextran as a proxy in the central channel of the microfluidic device confirm the establishment of stable chemical gradients within about 36 h (**Figure S1c**). Since the molecular weight of fluorescent dextran (70 kDa) is greater than that of FGF8 (23 kDa), RA (< 1 kDa), or other small molecules used in this work for modulating FGF / WNT signaling (see below), it is reasonable to assume that exogeneous signaling gradients could be established within the microfluidic channel within 36 h. Specifically, to derive PSM cells, H9 human embryonic stem cells (hESCs) in tissue culture plates are treated with a basal medium (BM) supplemented with CHIR99021 (or CHIR, a WNT activator) and LDN 193189 (or LDN, a BMP inhibitor), referred herein to as CL medium, for two days (from Day -2 to Day 0; **Figure 1b** and **Figure S1a&d**). On Day 0, hESCs differentiate into PSM cells expressing TBX6 (PSM-specific marker) but not SOX2 (pluripotency maker) or PAX3 (somite marker), with $TBX6^+$ PSM cell proportion around 94.4% (**Figure S1d**). $TBX6^+$ PSM cells co-express HOXC9 but not HOXC10, suggesting their thoracic or rostral lumbar axial identity (**Figure S1d**). PSM cells are

collected from tissue culture plates before re-seeding at a density of 15×10^6 cells mL^{-1} into the central channel of the microfluidic device on Day 0 in CL medium. Since only interior walls and bottom surfaces of micro-trenches are coated with Geltrex and thus adhesive to cells, whereas the other areas in the central channel are coated with bovine serum albumin (see **Methods**; **Figure S1a**), PSM cells loaded into the central channel are deposited only into micro-trenches and form initial PSM tissues (**Figure S1e**). On Day 1, Geltrex is loaded into the central channel to establish a Geltrex overlay for PSM tissues. Simultaneously, PD 173074 (or PD, a FGFR inhibitor; 400 nM) and RA (500 nM) are supplemented into the left reservoir of the central channel, hereafter designated as the rostral (R) end, while CHIR (10 μM), LDN (500 nM), and FGF8 (200 ng mL^{-1}) are added to the right reservoir, designated as the caudal (C) end (**Figure S1a**). This way, R-to-C gradient of RA and C-to-R gradients of FGF and WNT signals are established over the length of PSM tissues, mimicking morphogen environments experienced by PSM tissues *in vivo*.

Based on brightfield imaging of μSDM development, boundaries splitting PSM tissues into small compartments become visible in rostral μSDM regions from Day 4 onwards and gradually propagate caudally over time (**Figure S1e**). On Day 6, well-defined tissue boundaries separating individual rosette-like structures, indicating successful somite formation, are clearly notable in the rostral half of μSDM (**Figure S1e**). Immunostaining was conducted for TBX6 and PAX3 on μSDM (**Figure 1c** and **Figure S1g**). On Day 3, R-C patterned expression of TBX6 and PAX3 in μSDM emerges, with cells in the most rostral region expressing PAX3 but not TBX6 (**Figure 1c**). $PAX3^+$ somitic domain in μSDM expands caudally between Day 3 and Day 6, with concurrent caudal regression of $TBX6^+$ PSM region with a comparable speed (**Figure 1c&d**). Development of $PAX3^+$ somitic domain precedes somite formation in μSDM (**Figure 1c&d**). Nonetheless, on Day 3 local cellular compaction and re-organization become evident in rostral μSDM regions (**Figure 1c**), indicating initiation of MET and somite formation. On Day 6, well separated, mature $PAX3^+$ somites with an epithelial appearance and a closely packed circumferential ring of columnar-shaped cells surrounding small clumps of somitocoel cells are detectable across the entire rostral half of μSDM (**Figure 1d** and **Figure S1g**). Immunostaining of μSDM on Day 5 for HOXC9 and HOXC10 shows uniform HOXC9 expression yet with a few $HOXC10^+$ cells, confirming the thoracic or rostral lumbar axial identity of μSDM (**Figure S1h**).

Immunostaining of μSDM on Day 4 for SOX2 reveals a sprinkled distribution of a small amount of neural cells within μSDM (**Figure S1i**).

We next examined gene expression pattern in μSDM by dissecting μSDM into three equal-length segments and collecting them for RT-qPCR (**Figure S1j**). Consistent with immunostaining, rostral μSDM segments show relatively more notable expression of somite-related markers *PAX3*, *FOXC2*, *MEOX1*, and *TCF15*, whereas middle and caudal μSDM segments exhibit higher expression of PSM-related genes *HES7* and *TBX6* (**Figure S1j**).

To quantify spatiotemporal dynamics of somite formation, all somites in μSDM on Day 5 were split into two groups based on their relative distances to the caudal rosette formation front (**Figure. 1e**). Somites in the rostral half of the rosette-forming domain have an average area of 5,973 μm^2 (effective diameter of 87.2 μm; **Figure 1e**). Somites in the caudal half of the domain, which include relatively newly formed somites, show a smaller average area of 4,257 μm^2 (effective diameter of 73.6 μm; **Figure 1e**). Somite sizes in μSDM are thus comparable with those in CS9 - 10 human embryos (with an average diameter of 70 - 80 μm[10]). Circularities of somites in μSDM on Day 5 are comparable between the rostral and caudal halves of the rosette-forming domain (**Figure 1e**). Thus, our data suggest that nascent somites in μSDM might experience a growth process that increases their sizes but maintains their shape.

Confocal imaging of Day 5 μSDM confirms distant separations of neighboring somites and radial orientations of epithelialized somite boundary cells (**Figure 1f** and **Figure S1k**). *In vivo*, nascent boundaries between forming somites and the PSM are stabilized by epithelialization of somite boundary cells and assembly of extracellular matrix proteins in between[17]. Thus, we conducted immunostaining of μSDM for fibronectin and ZO1 on Day 3 and Day 5. There is no clear spatial pattern of fibronectin or ZO1 in μSDM on Day 3 (**Figure 1g**). On day 5, however, assembly of fibronectin is notable between adjacent somites, and ZO1 is evident demarcating the inner surface of epithelialized somite boundary cells, supporting the establishment of apical-basal polarity in individual somites (**Figure 1g**). An EdU labeling assay was performed on Day 5 and revealed proliferating cells in both the somite epithelium and somitocoel, supporting active proliferation of somitic cells that could contribute to somite size increases during μSDM development (**Figure S1l**).

Somite formation in μSDM is highly efficient and reproducible (**Figure S1f**), with about 93.8% samples successfully showing epithelialized rosette structures with well-separated tissue boundaries at the μSDM rostral ends.

To examine the robustness of μSDM, μSDM protocols were repeated using H1 hESCs and a hiPSC line (see **Methods**). Both H1 hESCs and the hiPSC line generate μSDM with R-C patterned TBX6 and PAX3 expression and well separated, $PAX3^+$ somites at the rostral ends (**Figure S2a**). Progression of somite formation front is comparable between H9 and H1 hESCs and the hiPSCs (**Figure S2b**). Areas of somites in μSDM generated from H9 and H1 hESCs appear to be greater than those from the hiPSC line (**Figure S2c**).

We also tested three different cell seeding densities (8×10^6 cells mL^{-1}, 15×10^6 cells mL^{-1}, and 25×10^6 cells mL^{-1}) for H9 hESCs (**Figure S2d**), with data showing no statistically significant difference in somite domain boundary position or somite area in Day 5 μSDM generated from these three different cell seeding densities (**Figure S2e&f**). This observation suggests that the cell seeding densities we used are already saturating, and active fluid flow inside the microfluidic device between Day 0 and Day 1 is effective in removing all excessive cells. Consistently, the thickness of PSM cell layers remaining in micro-trenches on Day 1 appears similar across the three tested cell seeding conditions (**Figure S2d**). It should be noted that local cell density near the two ends of the micro-trench could sometimes be higher, since these corners shield cells from medium flow that were used to remove excessive cells during cell seeding. Nonetheless, our data in **Figure S2d-f** support that somite formation in the μSDM is insensitive to the cell densities used in this study. The cell density of 15×10^6 cells mL^{-1} is used in the rest of this study.

Another mechanical factor, micro-trench width, was also explored (**Figure S2g**). Statistically comparable somite areas and somite domain boundary positions are observed in μSDM generated from 200 μm-, 300 μm-, and 400 μm-wide trenches (**Figure S2h&i**). The 200 μm-wide trenches, which were used in the rest of this study, give rises to approximately 2 rows of somites, whereas wider trenches produce more rows (**Figure S2g&j**). The width of 200 μm for micro-trenches is used in the rest of this study, in order to optimize model reproducibility because a narrower micro-trench can easily lead to air bubble entrapment during cell seeding and thereby cause tissue defects. Nevertheless, it is noteworthy that a 100 μm-wide micro-trench can lead to the development of a single linear array of somites in μSDM (**Figure S2k**). External

FGF8 gradients was also modulated for μSDM development (**Figure S2l-n**). Modulated FGF8 gradients generated by a lower FGF8 dosage (50 ng mL^{-1}) at the caudal end of μSDM tissues result in longer somite forming domains at SDM rostral regions (**Figure S2m**), even though somite areas appear insensitive to the two FGF8 gradient magnitudes tested (50 ng mL^{-1} *vs.* 200 ng mL^{-1}; **Figure S2n**).

As shown in **Figure S1e**, μSDM is compatible with live imaging. To exploit this advantage, we further conducted brightfield live imaging of developing μSDM (**Figure 2a** and **Supplementary Video 1**). We identified individual somites at the rostral μSDM region and tracked their development from Day 4 to Day 6 (**Figure 2a-c**). Time-lapse analysis reveals that nascent somites in caudal μSDM regions adopt a small area before growing between Day 4 to Day 6, while circularity of the somites maintains a relatively constant value throughout this time (**Figure 2b&c**), consistent with data in **Figure 1e**.

We further constructed a μSDM using a H9-H2B-GFP reporter line and tracked cellular dynamics in a forming somite at the rosette formation front *via* confocal imaging. MET-induced cellular compaction and epithelization are clearly evident in the forming somite, leading to a reduced in-plane tissue width and radially reoriented somitic cells setting up its boundary from adjacent somites (**Figure 2d** and **Supplementary Video 2**). Growth of nascent somites following their epithelialization was also observed, with dimensions of both somite and somitocoel increasing over time (**Figure S3a** and **Supplementary Video 3**). Interestingly, somitic cells in the epithelial ring constantly delaminate and move towards somitocoel cells as either single cells or cell clusters (**Figure S3b** and **Supplementary Video 4**), supporting continuous remodeling and dynamic cell movements within somites.

To examine the possible role and contribution of cell migration in somite formation and growth, we constructed μSDM tissues with H9 hESCs spiked with diluted H9-H2B-GFP reporter cells. By tracing positions of individual H2B-GFP^+ cells using live imaging, cell motility in μSDM between Day 3 and Day 4 was visualized and quantified (**Figure S3c**). Our data support no obvious long-range cell migration during μSDM development and thus exclude its possible role and contribution in somite formation and growth. Interestingly, a gradient in cell speed along the R-C axis of μSDM appears to exist, with cells in rostral μSDM regions moving slower than those in caudal domains, consistent with *in vivo* observations[18].

We also utilized a TCF/Lef H9 hESC reporter to track WNT activity in μSDM between Day 3 and Day 5 (**Figure 2e**). On Day 3 WNT activity is greater on the two ends of μSDM tissues, possibly due to greater local cell densities at these two regions, an artifact from the μSDM system (**Figure 2e**). On Day 4, WNT activity at caudal μSDM regions starts to appear greater than the rest of μSDM tissues (**Figure 2e**). Such WNT activity gradients along the R-C axis of μSDM become more prominent on Day 5 (**Figure 2e**).

Through employing an ERKKTR reporter, we quantified ERK activity during μSDM development (**Figure S3d-f**). On Day 5, the intensity of ERK signals first decreases and then increases along the R-C axis (**Figure S3f**), consistent with *in vivo* observations around the somite-PSM interface region[19]. As the caudal FGF8 dosage decreased from 200 ng mL^{-1} to 50 ng mL^{-1}, the position of minimum ERK activity shifts caudally, alongside a longer somite-forming regime in the rostral end of μSDM (**Figure S3e&f**).

Single-cell RNA-sequencing analysis

To investigate dynamics of μSDM development at the transcriptome level, single-cell RNA-sequencing (scRNA-seq) was conducted for Day 2, Day 3, Day 4, and Day 6 μSDM (n_{cell} = 14,513), respectively (**Figure 3a**). Uniform manifold approximation and projection (UMAP) dimension reduction was conducted for integrated scRNA-seq dataset combining data from all four time points, revealing five distinct mesodermal cell clusters annotated as 'caudal PSM / cPSM', 'rostral PSM / rPSM', 'nascent somite / N-SM', 'early somite / E-SM' and 'somite / SM' based on lineage marker expression patterns (**Figure 3b-d**, **Figure S4a-c**, and Mendeley **Table S1**). Consistent with immunostaining (**Figure S1i**), a small neural cell cluster was also identified (n_{cell} = 192, shown in **Figure S4a**); it was excluded from further analysis for clarity. We speculate that PSM cells seeded on Day 0 might contain a small number of neuromesodermal progenitors which can give rise to neuronal lineages.

Most cells in Day 2 μSDM are annotated as cPSM cells (**Figure 3e**). On Day 3, majority of cells in μSDM are identified as either rPSM or N-SM cells (**Figure 3e**). Most cells in Day 4 μSDM switch to E-SM identity before progressing to SM fate on Day 5 (**Figure 3e**). Both cPSM and rPSM clusters show upregulated expression of PSM-related genes such as *TBX6*, *MSGN1*, *RSPO3*, *DLL1*, and *HES7* (**Figure 3f** and **Figure S4b&c**). The rPSM cluster also shows upregulated expression of rostral PSM markers *MESP2* and *RIPPLY2* (**Figure 3f** and

Figure S4b&c). The somitic clusters N-SM, E-SM and SM all exhibit elevated expressions of somitic markers *TCF15* and *PAX3* (**Figure 3f** and **Figure S4b&c**). N-SM cluster also shows pronounced expression of *RIPPLY1*, while E-SM cluster is marked by greater expression of caudal somite/rostral PSM markers such as *FOXC2* compared to that of the SM cluster (**Fig. 3f** and **Figure S4b&c**). Expression of *HOX*5-9 genes, but not more caudal *HOX* genes, is evident in the mesodermal lineages in μSDM between Day 2 and Day 6 (**Figure S4d**), consistent with immunostaining data in **Figure S1h**. Notably, expression of *HOXC10* is evident in the small neural cluster (**Figure S4a**). Consistent with other *in vitro* human somitogenesis models[13], RA signaling-attenuating gene *DHRS3* is upregulated in cPSM, whereas RA synthesis-associated genes *ALDH1A2* and *RDH10* show elevated expression in somitic clusters N-SM, E-SM and SM (**Figure S4e**). *FGF3*/*8*/*17*/*18* and *DUSP6*, an FGF signaling target gene, mainly express in cPSM and rPSM (**Figure S4e**).

Cell clustering analysis using UMAP in **Figure 3a&b** shows cell fate transitions in μSDM from cPSM to rPSM and then somitic fates. Consistently, RNA velocity and pseudo-time analyses confirm a PSM-to-somite cell fate transition developmental trajectory (**Figure 3c&d**). Along the pseudo-time trajectory, PSM markers *TBX6*, *MSGN1*, and *RSPO3* are gradually down-regulated, whereas somitic markers *MEOX1*, *TCF15*, and *PAX3* are up-regulated (**Figure S4f**). Some rostral PSM and early somite markers, such as *MESP2* and *RIPPLY1*/*2*, are transiently up-regulated in rPSM and N-SM cells before decreasing rapidly in E-SM and SM cells (**Figure 3g** and **Figure S4f**).

We also conducted comparative transcriptome analysis, using scRNA-seq data from CS11 *cynomolgus* (*cy*) monkey embryo as a reference[20]. This comparative analysis reveals a reasonable overlap in UMAP projection between μSDM cells and cells from *cy* monkey PSM, nascent somite, and early somite clusters (**Figure 3h**). On the basis of most variable genes identified from the integrated scRNA-seq dataset combining μSDM and *cy* monkey cells, cPSM/rPSM, N-SM and E-SM/SM clusters in μSDM show the closest correlations with *cy* monkey PSM, nascent somite and early somite cells, respectively (**Figure 3i**). In addition, expression profiles of essential PSM and somitic markers in UMAP analyses show close similarities between μSDM cells and corresponding *cy* monkey somitogenesis-related cells (**Figure S4g**). We also compared the somite and PSM clusters of μSDM tissues and all lineages identified in the entire CS11 *cy* monkey embryo with UMAP projections and correlation

coefficients (**Figure S4h**). Consistently, the somite and PSM clusters in μSDM tissues show highest correlations with the paraxial mesoderm and PSM clusters in the CS11 *cy* monkey embryo, respectively (**Figure S4h**).

HES7 dynamics along the R-C axis

Somitogenesis *in vivo* is a rhythmic process that correlates temporally with a molecular oscillator, or the segmentation clock, acting in PSM cells[21]. The segmentation clock drives dynamic and periodic expression of a number of so-called 'clock' genes, including *HES7*, across the PSM in a C-to-R fashion (**Figure 4a**). To examine dynamic activities of clock genes in μSDM, a HES7 reporter hESC line[22] was used for μSDM development and imaged with confocal microscopy continuously between Day 2 and Day 4 (**Figure 4b&c** and **Supplementary Video 5**). Initially, HES7 traveling waves occur at both the rostral and caudal ends of μSDM, moving towards tissue center (**Figure 4b&c**). This observation is comparable to edge-to-center traveling waves noted in other somite organoids without R-C axial patterning[12]. After initial few oscillations, rostral-to-center HES7 traveling waves dim down by Day 3 (**Figure 4b&c**). The C-to-R HES7 traveling waves, however, persist, consistent with the establishment of an R-C axis in μSDM by Day 3 (**Figure 4b&c**). To corroborate this finding, we analyzed mean HES7 intensities in rostral, middle and caudal regions of μSDM (**Figure 4d**). HES7 oscillation in rostral μSDM regions flattens around Day 3, whereas HES7 intensities in middle and caudal μSDM regions continue undulating (**Figure 4d**). To quantitatively analyze C-to-R HES7 traveling waves, we extracted their time intervals and traveling speeds (**Figure 4b,e,f**). HES7 oscillation periods at the caudal μSDM end start from about 5 h, comparable with the period of human somite formation[22-24], and increases to about 6.8 h on the fifth observed traveling wave (**Figure 4e**). In contrast, HES7 oscillations at the caudal one-third position are notably slower, with its period starting from around 6.7 h and increasing up to 7 - 8 h (**Figure 4e**). The difference of oscillation clock periods between the two μSDM locations is consistent with decreasing HES7 traveling wave speeds over time (**Figure 4f**). The increasing oscillation clock periods at caudal μSDM locations are consistent with arrested segmentation clock when PSM cells in caudal μSDM regions transitioning to a somitic fate. The relatively shorter oscillation clock period at the μSDM caudal end is consistent with caudal-most cells in μSDM comparatively closer to the PSM identity. The spatial trend of increasing oscillation clock period

in μSDM along its C-to-R axis is also consistent with observations in animal[25] and *in vitro* models[14].

Biomechanics regulates somite formation

We next utilized μSDM to explore the mechanical regulators that contribute to somite formation and size regulation. To this end, we developed a theoretical model based on the most essential mechanical factors involved in somite formation. At the rostral end of the PSM where cells transition to somitic fates, the cells undergo MET and coalesce into a rosette-like structure that pulls apart from the PSM[26-30]. Somite-forming cell clusters at the rostral end of the PSM spontaneously become more compact, inducing a contractile eigen-strain (an inelastic deformation) on the PSM and producing strain energy. Since the somite-PSM mechanical interaction occurs mostly in the R-C axis, only the mechanical strain along this direction is considered in the model. When the strain energy exceeds surface energy required for the formation of a new somite-PSM boundary, the forming somite will delaminate from the rostral PSM and become a nascent somite (**Figure 5a**). As the length of PSM *in vivo* needs to be compatible with and thus constrained by adjacent tissues in the trunk, it is reasonable to assume that the total length of PSM is fixed during the formation of a new somite, which therefore provides a boundary condition for PSM deformation. Through an energetic analysis (see **Methods**), a scaling law that connects the dimension of nascent somite (d) with the length of PSM (L) is acquired as $d / \lambda = (L / \lambda)^{1/2}$, in which λ is a fitting parameter defined as $\lambda = 4\gamma / E\varepsilon^{*2}$, with γ being tissue surface energy density, E PSM tissue stiffness, and ε^* eigen-strain. Despite its simplistic nature, this scaling law agrees reasonably well with *in vivo* data from mouse[31,32], chick[32,33], and zebrafish[32,34] embryos (**Figure 5b**). Furthermore, the scaling law also fits reasonably well with data generated from μSDM, as well as data from human embryo[35] (**Figure 5b**). The *in vitro* human data appear distant from the rest of *in vivo* data because the length of micro-trenches and μSDM tissues is longer than those of the PSM *in vivo* (**Figure 5b**). It should be noted that the fitting parameter λ is dependent on specific datasets being fitted. Nonetheless, λ with closer values are observed for datasets from the same species.

To examine fidelity of the scaling law, biomechanical characterizations were conducted on μSDM. PSM tissue stiffness E in μSDM was determined using atomic force microscopy (**Figure 5c**). Eigen-strain ε^* was obtained by live imaging of the H2B reporter to record

compaction of forming somites (**Figure 5d**). Together with the λ used for best fitting of the scaling law with available μSDM somite size and PSM tissue length data, the surface energy density of PSM tissue was determined as $\gamma = 4.4$ pN μm^{-1}, which is of a comparable order of magnitude with that measured for zebrafish mesoderm[36] $\gamma = 20.5$ pN μm^{-1}.

We next conducted biomechanical, biochemical and genetic perturbation assays to examine how somite formation is regulated mechanically. A cell-stretching device was employed to apply periodic tensile straining with a period of 4 h on μSDM between Day 5 and Day 6 (see **Methods**; **Figure S5a-d**). Somite area in μSDM reduces to 80.7% of control values at a peak strain of 11% and further down to 74.3% under a peak strain of 28% (**Figure 5e**). Although it is not clear whether somites and PSM experience mechanical loading during the somitogenesis *in vivo*, there are animal and *in silico* studies indicating internal and external mechanical forces promoting somite boundary formation[37,38]. Our data further support that mechanical forces provide an integral driving force in controlling somite sizes. With intercellular adhesive interaction being an explicit parameter in our theoretical model that inhibits boundary formation, we supplemented ADH-1, an N-Cadherin inhibitor that blocks N-Cad-mediated cell-cell adhesion, into μSDM culture. Somite area in μSDM decreases by 26.9% compared to untreated controls, together with a longer rosette-forming rostral region in μSDM (**Figure 5f**). We next applied Y-27632 (ROCK inhibitor), cytochalasin D (actin polymerization inhibitor) and blebbistatin (myosin inhibitor) to inhibit intracellular cytoskeleton contraction machineries, which are known to be involved in epithelialization of somitic cells during the somitogenesis[39]. Somite formation in μSDM is largely abolished under these drug inhibition conditions (**Figure 5g**). Finally, we applied CRISPR-Cas9 gene editing tools to knockout (KO) *TCF15*, a gene involved in regulation of somitogenetic MET[40,41], in H9 hESCs (**Figure S5e**). In *TCF15*-KO mouse embryo, epithelialization of PSM tissue and thus somite boundary formation are disrupted, leading to musculoskeletal patterning defects[40,41]. Consistent with *in vivo* murine phenotype, *TCF15*-KO completely inhibits epithelialization and somite boundary formation in μSDM (**Figure 5h**).

DISCUSSION

Despite its importance in defining the segmented body plan in vertebrate species, it remains challenging to study somitogenesis. Stem cell-based somitogenesis models are promising for

advancing fundamental understanding of somitogenesis. However, existing hPSC-derived somitogenesis models lack extrinsic controls of bio-chemical or -mechanical cues, two essential mediators of somite formation, and as such they remain suboptimal for disentangling biochemical-biomechanical interactions that drive the sculpting of somites. The μSDM utilizes microfluidic morphogen gradients and microfabricated cell culture surfaces to effectively reconstruct the missing bio-chemical and bio-mechanical contexts of somitogenesis. Particularly, the μSDM focuses on modeling one important aspect of somitogenesis, somite boundary formation and associated morphogenetic cellular events, which eventually leads to delamination of new somites from the rostral end of the PSM. The μSDM effectively modularizes and thus is useful to decouple some critical molecular and cellular mediators of somitogenesis, such as external morphogen gradients and PSM tissue geometry. The modular bioengineering approaches utilized in the μSDM to decouple and independently control external biochemical gradients and tissue biomechanics are also useful for developing other controllable human embryo and organ models.

In our experiments we observed consistent lateral somite size under various widths of micro-trenches used for μSDM formation (**Figure S2g&j**). The lateral dimension of somites can be sensitive to various intrinsic and extrinsic factors. For example, tissue surface tension prefers an aspect ratio of unity and thus may help explain the uniform somite width across different trench geometries in the μSDM system. Furthermore, the somite growth and interaction with laterally neighboring tissues or tissue boundaries can also contribute to somite size regulation along the mediolateral axis.

A power-law scaling has also been previously reported on *in vivo* and explant somite data[6], where the authors investigated signaling dynamics within the PSM and attributed somite formation to biochemical interactions and specifications. In comparison, this study focused on the mechanical interaction between forming somites and the PSM. Nevertheless, the biochemical and biomechanical factors can be conjugated with MET being a consequence of upstream signaling events. The MET-associated eigenstrain has been assumed to be a constant for simplicity in our theory but can actually be correlated to signaling activities, and as such serve as a bridging element between biochemical and biomechanical mechanisms. Following this rationalization, it would then be of interest to investigate how cells in forming somites coordinate and orchestrate lineage fate regulation mediated by chemical signals, and the

boundary segmentation governed by mechanical forces. Notably, different developmental trajectories have been observed and proposed for rostral and caudal somitic mesoderm[43], which can potentially lead to distinct morphogenetic mechanisms and size regulations for rostral and caudal somites[6]. How the conclusions based on thoracic / lumbar mesodermal lineages in this study can be extended and generalized to more rostral or more caudal somites requires further examination.

In this study, we have developed a hPSC-based, R-C patterned somite formation model. Compared with other existing, free floating culture-based, human somitogenesis models, exogenous morphogen gradients and spatial tissue confinements that somites and the PSM experience *in vivo* are explicitly introduced and integrated in the μSDM system. We further constructed a mechanical theory to explain the size dependency between somites and the PSM. By exploiting the compatibility of μSDM with live imaging and biomechanical and molecular characterizations and perturbations, we explored and validated the regulatory role of biomechanics in somite boundary formation dynamics. We envision that the μSDM will be useful for deconstructing the regulation and dysregulation of somitogenesis and ultimately promoting both fundamental knowledge and modeling of human skeletal and muscular deformities.

Limitations of the study

Certain biomechanical aspects of somitogenesis, such as caudal elongation of the PSM, are not recapitulated in current μSDM. Even though HES7 oscillation dynamics along the R-C axis of the μSDM is shown, we are unable to explicitly correlate the segmentation clock with somite boundary formation dynamics in the temporal domain due to imaging limitations. It remains a future goal to apply the μSDM, in conjunction with high-resolution 4D imaging tools and signaling activity reporter lines, to study the interconnection between RA, FGF and WNT pathways and the segmentation clock and how such interactions regulate somite formation at both molecular and cellular scales.

Another important aspect about somitogenesis *in vivo* is the dynamic nature of morphogen gradients. As somites form and the PSM grows, FGF and WNT gradients shift caudally. Such dynamic signal gradients are not implemented in the current μSDM protocol but can be incorporated by adjusting morphogen dosages in medium reservoirs over time. As such,

different rates and patterns of morphogen gradient shifting can be examined, which should help reveal the dynamic signaling interactions during somite development.

Despite its simplistic nature, the theoretical model we report here for somite size regulation based on a fracture mechanics-based framework can properly explain a primary correlation between somite and PSM length scales, thus supporting a pivotal role of mechanics in regulating somite boundary formation. Nevertheless, our current model is unable to recapitulate some occasional asynchronies between peak PSM length and peak somite size[31,32], which suggests possible existence of secondary scaling. Mechanical gradients along the PSM and viscoelastic properties of mesodermal cells[42] might need to be considered to fully rationalize both long-range interactions among somites, PSM and neighboring tissues, and local cellular activities in the forming somite and rostral PSM region. Moreover, in our theoretical model, we assumed a fixed length for the PSM during somite formation. This is a simplified boundary condition to capture the most essential somite-PSM mechanical interactions. However, boundary conditions of the PSM *in vivo* are more complicated, given the axial elongation and complex tissue architectures and interactions near the caudal end of the PSM and tailbud.

ACKNOWLEDGEMENTS

We thank Dr. Miki Ebisuya at TU Dresden for valuable discussions and Usha Kadiyala at Univ. of Michigan for assisting confocal imaging. This work is supported by Michigan-Cambridge Collaboration Initiative, University of Michigan Mcubed Fund, University of Michigan Mid-career Biosciences Faculty Achievement Recognition Award, National Science Foundation (PFI-TT 2213845, I-Corps 2112458 and CBET 1901718), and National Institutes of Health (R21 NS113518, R21 HD105126, R21 NS127983, R21 HD109635, R21 HD105192 and R01 NS129850). We also thank the Single Molecule Analysis in Real-Time (SMART) Center at Univ. of Michigan, seeded by NSF MRI-R2-ID award DBI-0959823 to Dr. Nils G. Walter, as well as Damon Hoff for training, technical advice, and use of AFM. We acknowledge Michigan Advanced Genomics Core for scRNA-seq service, and Michigan Lurie Nanofabrication Facility for support in microfabrication. Research in the Pourquié laboratory was funded by a grant from the National Institutes of Health (5R01HD085121).

AUTHOR CONTRIBUTIONS

Y.L. and J.F. conceived and initiated the project; Y.L. designed, performed, and quantified most experiments, including scRNA-seq data analysis and interpretation; Y.L. conducted theoretical modeling; Y.S.K. generated KO hPSC lines; X.X. helped with scRNA-seq data analysis; Y.M. developed ERKKTR reporter line; N.K. and S.S. helped repeat experiments; R.Z.Y. helped with microfluidic device fabrication; O.P. provided HES7 reporter line; Q.Y. and O.P. helped with data interpretation and experimental designs; Y.L. and J.F. wrote manuscript. J.F. supervised the study. All authors edited and approved the manuscript.

DECLARATION OF INTERESTS

The authors declare no competing interests.

FIGURE LEGENDS

Figure 1. A hPSC-based, microfluidic somite development model (μSDM). **a**, (top) Sagittal view of a vertebrate embryo showing somite formation from the presomitic mesoderm (PSM), regulated by opposing morphogen gradients along the rostral (R)-caudal (C) axis. The μSDM is developed to model somite formation from the thoracic / lumbar PSM region, as marked in the dashed box. (Bottom) Transverse section of the trunk showing a somite (cyan) mechanically confined by adjacent tissues during its development. **b**, Schematics showing μSDM development protocol. See **Methods** for μSDM design considerations. hPSC-derived PSM tissues are confined in microfabricated open trenches, before 3D gel overlay and microfluidic morphogen gradients are imposed on PSM tissues to establish an R-C axis and drive spontaneous somite formation, beginning rostrally and extending caudally. **c**, Representative stitched confocal micrographs showing μSDM on Day 3 and Day 5 stained for PAX3 and TBX6. Cell nuclei were counterstained with DAPI. Zoom-in views of boxed regions are shown at the bottom. Scale bars, 100 μm for full-tissue images and 50 μm for zoom-in images. **d**, Bar plot showing spatial patterns of somite formation and PAX3 and TBX6 expression in μSDM as a function of culture day as indicated. Data from the same microfluidic device are plotted on the same row with the same shape code. $n_{\mu SDM} \geqslant 10$ for each day, and data are plotted as the mean ± s.d. **e**, (top) Area and circularity of individual somites between the rostral end and rosette front in μSDM on Day 5. (bottom) Data from the rostral and caudal halves within this somite formation regime are grouped and analyzed respectively. Data from the same micro-trench are plotted on the same column while data from the same microfluidic device are plotted with the same shape code. $n_{\mu SDM} = 12$, and $n_{somite} = 140$ for rostral halves and $n_{somite} = 163$ for caudal halves. Boxes and bars indicate interquartile ranges and median values, respectively, and squares and error bars indicate the mean ± s.d. Two-sample *t*-tests for somite area comparison ($P = 1.5\times10^{-13}$) and for somite circularity comparison ($P = 0.20$). **f**, Representative confocal Z-stack images showing individual somites in μSDM on Day 5 stained with DAPI. Scale bar, 100 μm. **g**. Representative confocal micrographs showing rostral regions of μSDM on Day 3 and Day 5 stained for fibronectin and ZO1 as indicated. Scale bars, 100 μm. **See also Figures S1 and S2.**

Figure 2. Cellular dynamics and WNT activities during μSDM development. **a**, Brightfield imaging of the rostral region of a single μSDM between Day 4 and 6, revealing spontaneous somite formation, beginning rostrally and extending caudally. **b**, Spatiotemporal distributions of the area (top) and circularity (bottom) of individual somites in the same single μSDM between Day 4 and 6 based on brightfield imaging. Each data point is from a single somite. **c**, Dynamic evolvements of area (top) and circularity (bottom) of individual somites between Day 4 and 6. Each light grey line represents an individual somite while black line shows the mean value. $n_{somite} = 12$. **d**, Confocal imaging of a H2B reporter line revealing sagittal view of cell dynamics in a forming somite close to the rosette front, which shows cellular compaction and reorganization, leading to the formation of a somite with an epithelial appearance and a closely packed circumferential ring of columnar-shaped cells, elongated in the radial direction. The rostral and caudal ends of the forming somite are marked by dashed lines. **e**, (left) Representative stitched epifluorescence micrographs of μSDM developed from a TCF/Lef reporter between day 3 and day 5, and (right) normalized WNT signal intensities across TCF/Lef reporter-based μSDM between day 3 and day 5. Each light grey line represents an individual μSDM while black line shows the mean value. $n_{\mu SDM} = 6$. Scalbars, 100 μm (**a & d**) and 200 μm (**e**). **See also Figures S3.**

Figure 3. Single-cell transcriptomic analysis of μSDM. **a-d**, UMAP embedding of integrated single-cell transcriptome dataset of μSDM on Day 2 ($n_{cell} = 3{,}259$), Day 3 ($n_{cell} = 3{,}808$), Day 4 ($n_{cell} = 3{,}620$) and Day 6 ($n_{cell} = 3{,}634$), color-coded by μSDM culture time (**a**), cell identity annotation (**b&c**) and pseudotime (**d**). RNA velocity vectors projected onto UMAP embeddings in **c** show major cell progression directions in transcriptional space. Start and endpoints of arrows indicate observed-current and predicted-future cell states, respectively. **e**, Proportions of different cell types in μSDM over time. **f**, Dot plot showing expression of key marker genes across different cell clusters in μSDM. Dot sizes and colors indicate proportions of cells expressing corresponding genes and their averaged scaled values of log-transformed expression, respectively. **g,** Expression dynamics of key marker genes in μSDM along the pseudotime trajectory corresponding to **d**. Color bars above the heat map indicate pseudotime and cell identity as indicated. **h,** (top) UMAP projection of integrated scRNA-seq dataset from μSDM

and somitogenesis-related cells from a CS11 monkey embryo[20]. (middle/bottom) UMAP projections of datasets from μSDM and the CS11 monkey embryo, separated from the integrated UMAP plot on the top, with cell identity annotations indicated. **i,** Pearson's correlation analysis of μSDM cell clusters with somitogenesis-related cell clusters in the CS11 monkey embryo. Correlation coefficients between indicated μSDM and monkey cell clusters are calculated based on variable genes identified from the μSDM/monkey somitogenesis-related cell clusters (Mendeley **Table S2**). Cpsm, caudal PSM; Rpsm, rostral PSM; N-SM, nascent somite; E-SM, early somite; SM, somite. **See also Figure S4.**

Figure 4. *HES7* dynamics during μSDM development. **a**, Schematics of oscillation and propagation of *HES7* expression in the PSM during somitogenesis *in vivo*. **b**, Time-lapse images showing development of μSDM using a *HES7* reporter line between $t = 48 – 96$ h. A dashed curve marks a non-oscillating region at the rostral end of μSDM. Traveling waves of *HES7* expression are marked by dashed lines with arrows. Oscillation periods at the caudal end ($P1 – P5$) and the caudal one-third point ($P1^* - P5^*$), and the wave speed between the two points ($V1-V6$) are marked and defined, respectively. Scale bar, 200 μm. **c**, Heatmap showing *HES7* intensity along μSDM length over time. *HES7* intensity is averaged across the micro-trench width. **d**, Mean *HES7* expression within the rostral, middle, and caudal one-third of μSDM as a function of time. Light grey lines indicate *HES7* expression dynamics of individual μSDM while colored lines represent averages. $N_{\mu SDM} = 3$, and shaded areas indicate s.d. **e**, Oscillation period of *HES7* at the caudal end ($P1 – P5$) and the caudal one-third point ($P1^* - P5^*$). Data are plotted as the mean ± s.d., with $n_{\mu SDM} = 3$. **f**, Propagation velocity of *HES7* expression waves traveling from the caudal end to the caudal one-third point. Data are plotted as the mean ± s.d., with $n_{\mu SDM} = 3$.

Figure 5. Mechanical modeling, characterization and perturbation of μSDM development. **a**, Schematics of MET-driven tissue deformation and nascent tissue boundary formation at the rostral PSM, leading to a forming somite delaminating from the PSM. **b**, Scaling law between length scales of a newly formed somite and the PSM derived from mechanical modeling, fitted with *in vivo* data from the zebrafish mouse[31,32], chick[32,33], zebrafish[32,34] and human embryos,[35] and μSDM data. Data from μSDM were obtained from $n_{\mu SDM} = 26$ on Day 4, 5 and 6. **c**,

Young's modulus measured by atomic force microscopy (AFM) for μSDM regions with and without rosette formation as indicated on Day 5. $N_{\mu SDM} = 2$. **d**, (left) Live imaging of μSDM development from a H2B reporter line showing compaction of a single forming somite between Day 4 and 5. Scale bar, 20 μm. (right) Quantitative data showing projected area compaction of single forming somites in μSDM. $N_{\mu SDM} = 5$. **e**, (left) Representative confocal micrographs showing μSDM on Day 6 stained with DAPI under control and 28% strain conditions. (right) Quantitative data showing projected area of individual somites in μSDM as a function of mechanical strains. Two-sample *t*-tests for control *vs.* 11% strain ($P = 8.8\times10^{-14}$), control *vs.* 28% strain ($P = 1.3\times10^{-25}$), and 11% strain *vs.* 28% strain ($P = 6.4\times10^{-3}$). In control group, $n_{\mu SDM} = 36$ and $n_{somite} = 507$; in 11% strain group, $n_{\mu SDM} = 18$ and $n_{somite} = 326$; in 28% strain group, $n_{\mu SDM} = 18$ and $n_{somite} = 376$. **f**, Impact of ADH-1 treatment on μSDM development. (left) Representative confocal micrographs showing μSDM on Day 5 stained with DAPI under control and ADH-1 treatment conditions. (right) Quantitative data showing projected somite area and rosette formation front in μSDM on Day 5 under control and ADH-1 treatment conditions as indicated. For somite projected area data, $n_{\mu SDM} = 14$ and $n_{somite} = 171$ for control group and $n_{\mu SDM} = 13$ and $n_{somite} = 207$ for ADH-1 treatment group. Two-sample *t*-test for the two groups ($P = 3.8\times10^{-14}$). For rosette front data, $n_{\mu SDM} = 15$ for control group and $n_{\mu SDM} = 16$ for ADH-1 treatment group. Two-sample *t*-test for the two groups ($P = 0.029$). Somite area data in **e** and **f** were measured from full tissues. **g**, Impact of Y-27632 (Y27), cytochalasin D (CytoD) and blebbistatin (Blebb) treatment on μSDM development. (left) Representative confocal micrographs showing rostral regions of μSDM on Day 5 stained with DAPI under different conditions as indicated. While arrowhead marks occasional rosette-like cell organization under Blebb treatment. (right) Quantitative data showing rosette formation front in μSDM on Day 5 under different conditions as indicated. $n_{\mu SDM} = 13$ (control), $n_{\mu SDM} = 20$ (Y27), $n_{\mu SDM} = 18$ (CytoD), and $n_{\mu SDM} = 18$ (Blebb). Two-sample *t*-tests: control *vs.* Y27, $P = 4.2\times10^{-11}$; control *vs.* CytoD, $P = 2.1\times10^{-10}$; control *vs.* Blebb, $P = 4.0\times10^{-9}$. **h**, Effect of *TCF15*-KO on μSDM development. (top) Representative confocal micrographs showing μSDM on Day 5 stained with DAPI under different conditions as indicated. (bottom) Quantitative data showing rosette formation front in μSDM on Day 5 under different conditions as indicated. $n_{\mu SDM} = 18$ for both control and *TCF15*-KO conditions. Two-sample *t*-test between control vs. *TCF15*-KO conditions ($P < 0.001$). In **c**, **d** and all somite area quantification plots in **e**-**h**, boxes and bars

indicate interquartile ranges and median values, respectively, and squares and error bars indicate the mean ± s.d. In rosette front quantification plots, bars and error bars indicate the mean ± s.d. Scale bars in **e**-**h**, 100 μm. **See also Figure S5.**

STAR METHODS

RESOURCE AVAILABILITY

Lead contact

Further information and requests for resources and reagents should be directed to and will be fulfilled by the lead contact, Jianping Fu (jpfu@umich.edu).

Materials availability

The cell lines generated in this study will be distributed upon request to other research investigators under a Material Transfer Agreement.

Data and code availability

- Single-cell RNA-seq data have been deposited at GEO and are publicly available as of the date of publication. Accession numbers are listed in the key resources table. Supplementary Tables S1 - S3 have been deposited at Mendeley and are publicly available as of the date of publication. The DOI is listed in the key resources table.
- This paper does not report original code.
- Any additional information required to reanalyze the data reported in this paper is available from the lead contact upon request.

EXPERIMENTAL MODEL AND STUDY PARTICIPANT DETAILS

Cell lines

Human pluripotent stem cell (hPSC) lines used in this study include both human embryonic stem cells (H9, WA09, WiCell, NIH registration number: 0062; H1, WA01, WiCell, NIH registration number: 0043) and human induced pluripotent stem cells (NCRM1 hiPSC, a HES7-Achilles;pCAG-H2B-mCherry reporter[22]). H2B reporter, TCF/Lef:H2B-GFP reporter[7], and *TCF15*-knockout hPSC lines developed based on H9 hESCs and an HES7-Achilles;pCAG-H2B-mCherry;ERKKTR-Halo reporter developed based on iPSC are also used in this study. All protocols with hPSCs have been approved by the Human Pluripotent Stem Cell Research Oversight Committee at the University of Michigan, Ann Arbor. All hPSC lines have been authenticated by original sources as well as in-house by immunostaining for pluripotency markers and successful differentiation to the three germ layers. All hPSC lines are maintained in

a feeder-free system for at least ten passages and authenticated as karyotypically normal. Karyotype analysis is performed by Cell Line Genetics. All hPSC lines are tested negative for mycoplasma contamination (LookOut Mycoplasma PCR Detection Kit, Sigma-Aldrich).

Cell culture

All hPSC lines are maintained in a standard feeder-free culture system using mTeSR medium (mTeSR; STEMCELL Technologies). H9 and H1 hESCs are cultured in tissue culture plates coated with lactate dehydrogenase-elevating virus (LDEV)-free, hESC-qualified reduced growth factor basement membrane matrix Geltrex (Thermo Fisher Scientific; derived from Engelbreth-Holm-Swarm tumors similarly to Matrigel). NCRM1 hiPSCs are cultured in tissue culture plates coated with hESC-qualified LDEV-free Matrigel (Thermo Fisher Scientific). Cell culture is visually examined during each passage to ensure absence of spontaneously differentiated, mesenchymal-like cells in culture. hPSCs between P50 and P70 are used for experiments.

Generation of H2B-eGFP hESCs

A CAG-H2B-eGFP H9 hESC line is generated as previously reported[7]. Specifically, H2B-eGFP (Addgene ID: 32610) is PCR amplified and cloned into an ePiggyBac vector with a constitutively active puromycin selection cassette[44]. The plasmid is co-transfected with pCAG-PBase (ePiggyBac transposase helper plasmid, provided by Dr. A.H. Brivanlou at Rockefeller Univ.) into H9 hESCs using Lipofectamine Stem (Thermo Fisher Scientific, STEM00003). Two days after transfection, CAG-H2B-eGFP H9 hESCs are selected with puromycin (1 μg mL^{-1}; Thermo Fisher Scientific, A1113803) for 7 days.

Generation of HES7-Achilles;pCAG-H2B-mCherry;ERKKTR-Halo iPSCs

To make the cell line that reports ERK activity, we inserted the ERKKTR sequence[45] under a constitutively expressed promoter in the safe harbor AAVS1 locus of the HES7-Achilles;pCAG-H2B-mCherry reporter cell line[22]. We used a previously described approach[46]. In brief, we cloned the ERKKTR-Halo-t2a-H2B-mCherry sequence into the AAVS1-pCAG vector (Addgene, 80490) and co-transfected it along with the pXAT2 vector (Addgene, 80494) into cells by nucleofection (Lonza, VPH-5022) using the NEPA 21 electroporator. 1 day after nucleofection, we selected positive clones by supplementing mTeSR1 with puromycin (0.5 μg

672 ml^{-1}, Sigma-Aldrich, P7255) for a total of 4 days. Single colonies with homozygous insertion
673 were confirmed by PCR and expanded further.
674
675 **Generation of *TCF15*-KO hESCs**
676 *TCF15*-KO H9 hESCs are generated by targeting exon 1 of *TCF15* gene using CRISPR/Cas9-
677 medited genome editing. Guide RNAs (gRNA) targeting the upstream and downstream introns
678 spanning exon 1 of *TCF15* gene are designed using E-CRISP design tool (www.e-crisp.org/E-
679 CRISP/designcrispr.html). The gRNAs are cloned into PX459-2A-Venus. The list of gRNAs is
680 listed in **Mendeley Table S3**. The gRNAs are transfected into H9 hESCs and after 48 h, venus-
681 positive cells are sorted by fluorescence-activated cell sorting (FACS). Sorted cells are plated on
682 a tissue culture plate as single cells. After 7 days, individual hESC clones are isolated and are
683 further genotyped for exon deletion by PCR using the primers listed in **Mendeley Table S3**.
684
685 **METHOD DETAILS**
686 **Microfluidic device fabrication**
687 The microfluidic device for μSDM development consists of a polydimethylsiloxane (PDMS)
688 structural layer attached to a PDMS micro-trench layer (**Figure S1a&b**). The PDMS structural
689 layer is generated by mixing PDMS curing agent and base polymer (Sylgard 184; Dow Corning)
690 at a ratio of 1:10 before casting PDMS prepolymer onto a microfabricated silicon mold and
691 baking at 110°C for 1 h. Medium reservoirs (6 mm in diameter) and a loading port (1 mm in
692 diameter) are then punched into the PDMS structural layer with Harris Uni-Core punch tools
693 (Ted Pella).
694 To fabricate the micro-trench layer, PDMS molds are first generated by casting PDMS
695 prepolymer with a 1:10 curing agent-to-base polymer ratio onto a microfabricated silicon mold
696 and baking at 110°C for 1 h. Surfaces of PDMS molds are treated with air plasma for surface
697 activation before silanization (Sigma-Aldrich, 448931-10G). The PDMS molds are then placed
698 on PDMS prepolymer (1:20 curing agent-to-base polymer ratio) casted on a glass coverslip,
699 before being baked at 110°C for 1 h. The PDMS micro-trench layers are then obtained after
700 peeling off the molds.
701 Prior to experiments, micro-trenches are filled with 1% Geltrex (*v*/*v*) at 4°C overnight to
702 coat their interior walls and bottoms. The PDMS micro-trench layers are then immersed in 1%

bovine serum albumin (BSA; Thermo Fisher Scientific) solution at room temperature for 30 min. On Day 0, the PDMS structural layer is physically attached to the PDMS micro-trench layer, with micro-trenches visually aligned to be at the center of the microchannel in the PDMS structural layer.

The design of the PDMS structural layer includes three parallel channels that are partitioned by circular support posts (**Figure S1a&b**). The central channel in the PDMS structure layer is used for establishing chemical gradients through passive diffusion. Circular support posts separating the central channel from the other two channels are designed to constrain Geltrex solutions loaded into the central channel (see more information below) as well as to prevent air bubble trapping in the central channel during cell and Geltrex loading. The width and depth of micro-trenches are chosen to minimize air bubble trapping in the trenches during cell seeding, whereas the length of micro-trenches, and therefore of μSDM tissues, is chosen to amplify the difference in morphogen concentration between two ends of μSDM tissues.

Development of μSDM

Between Day -2 and Day 0, colonies of hPSCs in tissue culture plates are treated with a basal medium supplemented with CHIR99021 (CHIR; 10 μM, STEMCELL Technologies) and LDN-193189 (LDN; 500 nM, STEMCELL Technologies), which is referred to as CL medium. The basal medium consists of Essential 6 (Gibco), GlutaMax (Gibco) and antibiotic/antimycotic (Gibco). On Day 0, cells in tissue culture plates are dissociated using Accutase (Sigma-Aldrich) at 37°C for 8 min before being suspended in DMEM/F12 (GIBCO) as single cells. Cells are then centrifuged and re-suspended in CL medium supplemented with Y27632 (10 μM, Tocris) at a density of 15×10^6 cells mL^{-1}. 10 μL cell suspension is then introduced into the central channel of the microfluidic device through its loading port on Day 0. Cells are allowed to settle into micro-trenches for 3 h, before the two medium reservoirs of the central channel are filled with CL medium supplemented with 10 μM Y27632. On Day 1, after aspirating culture medium from the central channel, 70% Geltrex (diluted in basal medium) is introduced into the central channel to establish a 3D culture environment. Starting from Day 1, the rostral reservoir connecting the central channel is filled with basal medium supplemented with retinoic acid (500 nM, STEMCELL Technologies) and PD173074 (400 nM, Tocris Bioscience), while the caudal

reservoir is filled with CL medium supplemented with FGF8 (200 ng mL^{-1}, PEPROTECH). Culture medium is then replenished daily.

Immunocytochemistry

To stain μSDM tissues, the PDMS structural layer is first removed from the microfluidic device prior to fixation of μSDM tissues. Cells and tissues are fixed in 4% paraformaldehyde (buffered in 1× PBS) for 12 h, and permeabilized in 0.1% SDS (sodium dodecyl sulfate, dissolved in PBS) solution at room temperature for 3 h. Samples are then blocked in 4% donkey serum (Sigma-Aldrich) at 4°C for 24 h, followed by incubation with primary antibody solutions at 4°C for 24 h. Samples are then labelled with donkey-raised secondary antibodies (1:400 dilution) at 4°C for 24 h. 4',6-diamidino-2-phenylindole (DAPI; Thermo Fisher Scientific) is used for counterstaining cell nuclei. Both primary and secondary antibodies are prepared in 4% donkey serum supplemented with 0.1% NaN_3. All primary antibodies used in this study are listed in **Key resources table**.

To clear μSDM tissues optically after immunofluorescence staining, μSDM tissues are incubated for 60 min in a refractive index (RI)-matching solution comprising 6.3 mL ddH_2O (double distilled water), 9.2 mL OptiPrep Density Gradient Medium (MilliporeSigma), 4 g N-methyl-D-glucamine (MilliporeSigma), and 5 g diatrizoic acid (MilliporeSigma)[47]. For each μSDM sample, 50 μL of RI-matching solution is used.

Microscopy

Fluorescence imaging is conducted using an Olympus DSUIX81 spinning-disc confocal microscope. To image entire μSDM tissues, an array of partially overlapping images (50% overlap) are taken to cover entire μSDM tissues. Recorded images are stitched together using ImageJ plugin MIST. For *z*-stacking, images are acquired with a slice thickness of 0.5 μm. Low-magnification brightfield images are acquired using a Labomed TCM 400 inverted microscope equipped with a UCMOS eyepiece camera (Thermo Fisher Scientific). Brightfield live imaging is conducted using an inverted epifluorescence microscope (Zeiss Axio Observer Z1; Carl Zeiss MicroImaging) enclosed in an environmental incubator (XL S1 incubator, Carl Zeiss MicroImaging), maintaining cell culture at 37°C and 5% CO_2. Fluorescence live imaging is conducted using an Olympus FV1200 confocal microscope equipped with a TOKAI HIT

stage-top incubator to maintain cell culture at 37°C and 5% CO_2. For z-stacking of fluorescence live imaging, images with a slice thickness of 5 μm are acquired.

Morphology quantifications

To quantify somite morphology, only rosette structures that show discernable outer and inner surfaces of the enveloping epithelium layer are selected. In ImageJ, an outline is manually drawn along the outer surface of rosettes, and morphological features such as area and circularity are automatically computed and extracted through the Measurement function of ImageJ.

Quantification of μDSM efficiency

Quantification of μSDM is based on visual examination of brightfield images recorded for μSDM tissues on Day 5. μSDM with discernible rosette structures are counted as successful μSDM. Tissues with structural defects, which could be due to failed cell seeding or gel loading, are excluded from statistical analysis.

EdU labeling assay

To visualize cell proliferation in μSDM, we performed an EdU labeling assay for μSDM tissues on Day 5. Specifically, we used Click-iT EdU Alexa Fluor 488 Imaging Kit (Thermo Fisher Scientific) by following the manufacturer's instructions. On Day 5, PDMS microfluidic devices are removed. μSDM tissues are then incubated with basal medium supplemented with EdU (20 μM) for 2 h before being fixed, permeabilized, and incubated with the Click-iT reaction cocktail for 30 min. Cell nuclei are counterstained with DAPI. μSDM are then imaged by a confocal microscope.

ERK activity quantification

To visualize and quantify spatial distribution of ERK activity, we employed the HES7-Achilles;pCAG-H2B-mCherry;ERKKTR-Halo reporter line to generate a μSDM. The Janelia Fluor HaloTag (Promega, 1:1000) dye was supplemented into the system on Day 1 along with gel loading. On Day 5 the samples were fixed and imaged. H2B signal is used as a mask to extract nuclear expression of ERKKTR, and ERK activity is defined as:

$$\text{ERK activity} = 1 - \text{nuclear ERKKTR expression} / \text{total ERKKTR expression}.$$

The entire μSDM is partitioned into 5 equal-length regions, and the mean ERK activity in each region is extracted.

Cell motility tracking assay

H2B-eGFP hESCs and non-fluorescent hESCs are both treated with CL medium for 2 days before they are mixed at a ratio of 1:200 and seeded into the microfluidic device on Day 0. Migration of single H2B-eGFP hESCs is monitored using epifluorescence microscopy between Day 3 to Day 4 during the development of μSDM. Images are taken once every 30 min. The motion of H2B signals is tracked by the TrackMate Plugin of ImageJ. Cell migration tracks with duration more than 10 frames are adopted for analysis.

RNA isolation and RT-qPCR analysis

On Day 5, the PDMS structural layer is first removed from the microfluidic device. μSDM tissues remaining on the PDMS micro-trench layer are cut into three even segments using a surgical scissor. RNA from each tissue segment is extracted using RNeasy mini kit (Qiagen) following the manufacturer's instructions. A CFX Connect SYBR Green PCR Master Mix system (Bio-Rad) is used for RT-qPCR. An arbitrary Ct value of 40 is assigned to samples in which no expression is detected. Relative expression levels are determined as $2^{-\Delta\Delta Ct}$ with the corresponding s.e.m. Human GAPDH primer is used as endogenous control. All fold changes are defined relative to undifferentiated H9 hESCs. All analyses are performed with at least three biological replicates and two technical replicates. All primers are obtained from Ref[10,23,48] and listed in **Mendeley Table S3**.

Single-cell dissociation and RNA-sequencing

To dissociate μSDM tissues into single cells, the PDMS structural layer is first removed from the microfluidic device, to expose and release μSDM tissues from micro-trenches. μSDM tissues are first cut into small pieces using a surgical knife and then incubated with Accutase for 2 - 3 h to obtain dissociated single cells. For scRNA-seq analysis of μSDM tissues at different time points, dissociated single cells from Day 2, 3, 4 and 6 μSDM tissues are harvested from 18 μSDM tissues. Dissociated single cells are collected into PBS containing 1% BSA before being centrifuged at 300 g for 5 min. Resultant cell pellets are re-suspended into single cells in PBS

containing 1% BSA. Within 1 h after cell dissociation, cells are loaded into the 10× Genomics Chromium system (10× Genomics). 10× Genomics v.3 libraries are prepared according to the manufacturer's instructions. Libraries are then sequenced using paired-end sequencing with a minimum coverage of 20,000 raw reads per cell using Illumina NovaSeq-6000. ScRNA-seq data are aligned and quantified using Cell Ranger Single-Cell Software Suite (v.3.1.0, 10× Genomics) against the Homo sapiens (human) genome assembly GRCh38.p13 from ENSEMBL.

Data integration, dimensionality reduction, and clustering

Analysis of scRNA-seq data and integration of scRNA-seq datasets are performed using R package Seurat (v.3.0.0.0, https://satijalab.org/seurat/)[49]. Default setups in Seurat are used unless noted otherwise. Briefly, each scRNA-seq dataset is filtered first based on the total number of genes detected and the percentage of total mitochondrial genes. Gene expression is then calculated by normalizing the raw count with the total count before multiplying by 10,000 and log-transformed. Top 2,000 highly variable genes are identified for each dataset using FindVariableFeatures. Datasets from different time points are then merged together. Cell cycle is regressed out based on cell cycle scores using CellCycleScoring during the data scaling process using SCTransform. PCA analysis (RunPCA) is then performed on filtered data followed by embedding into low dimensional space with Uniform Manifold Approximation and Projection (UMAP; RunUMAP) using dim 1:50, min.dist = 0.3, and n.neighbors = 5. Identification of cell clusters by a shared nearest neighbor (SNN) modularity optimization-based clustering algorithm is achieved using FindClusters with a resolution 0.2. To integrate multiple scRNA-seq datasets, count matrices of different datasets are first filtered and normalized separately before being integrated using IntegrateData. Integrated scRNA-seq dataset is analyzed following the standard Seurat pipeline. Annotation of cell clusters is based on expression of canonical lineage marker genes. The neural cluster identified is removed from further analysis. Differentially expressed genes (DEGs) are identified using FindAllMarkers, with min.pct = 0.1 and logfc.threshold = 0.25. Identified DEGs and their expression levels are summarized in Mendeley **Table S1**. Dot plots and feature plots are generated using DotPlot and FeaturePlot in Seurat, respectively. Heatmaps are plotted based on relative expression (*Z*-score) of top-20 gene signatures to distinguish each cell cluster under comparison.

RNA velocity analysis

FASTQ files generated by the Cell Ranger pipeline are used for RNA velocity analysis. Genome annotations GRCh38 are used for counting spliced and unspliced mRNA in each single cell. First, loompy fromfq is applied, with human genome assembly GRCh38 passed as an annotation, to generate the loom files containing both spliced and unspliced mRNA counts. Python package UniTVelo (v.0.2.2, https://unitvelo.readthedocs.io/en/latest/) is adopted to perform RNA velocity analysis[50]. Function 'scv.pl.velocity_embedding_stream' is used to project RNA velocities onto UMAP plots. All default parameters are used unless noted otherwise.

Trajectory inference and pseudotime analysis

R-package Slingshot is used for trajectory inference of the PSM-somitic cell lineage development[51]. Specifically, the merged dataset in Seurat is used as input to Slingshot. The rPSM cluster is assigned as the starting cell state. To visualize gene expression dynamics, expression levels of selected genes are first plotted along the pseudotime trajectory, and then fitted onto principal curves, which are further plotted as a function of pseudotime using plotSmoothers.

Comparison with monkey data

Three cell clusters ("PSM", "Somitomere", which is renamed in this study as "Nascent somite", and "Early somite") are chosen from the scRNA-seq dataset of a CS11 monkey embryo[20]. Monkey gene names are first projected to human ortholog gene names before the monkey dataset is integrated with the μSDM dataset using function IntegrateData with normalization.methd = "SCT". UMAP embedding is then computed with first 30 principal components. Pearson's correlations between cell clusters from the monkey CS11 dataset and the merged μSDM dataset are calculated using function cor. Note that in their full embryo data, no detailed annotation for the mesodermal lineages is provided, and all PSM and somitic lineages are grouped as "PSM" and "Para.Meso" clusters, respectively. To mimic their annotation in the comparison with full embryo data, we also grouped our "N-SM" (nascent somite), "E-SM" (early somite), and "SM" (somite) clusters together as a "somite" cluster, and combined our "cPSM" (caudal PSM) and "rPSM" (rostral PSM) into a "PSM" cluster.

Theoretical modeling of somite boundary formation

Given the physical similarity between somite segmentation and mechanical fracture, a fracture mechanics-based theory is developed to rationalize somite boundary formation process (**Fig. 5a**). In the model, the PSM is regarded as a homogeneous one-dimensional rod with length L, cross-sectional area A and *Young*'s modulus E. At the rostral end of the PSM tissue, a somite forming region with length d experiences an eigen-strain $\varepsilon^* < 0$, resulted from MET-induced cellular compaction. Specifically, a negative eigen-strain, describing an inelastic shrinking deformation, is resulted from tissue re-organization, which can persist under stress-free condition. Assuming that the PSM rod is fixed on both its ends, a simplification of the *in vivo* boundary condition resulted from tissues surrounding the PSM and somites, the strain energy in the entire PSM is calculated as $\psi^e(d) = EA(\varepsilon^*)^2 d^2 / (2L)$. When a somite segmentation is initiated, a nascent somite delaminates from the rostral PSM region, releasing strain energy. However, this nascent somite formation leads to additional surface energy associated with newly generated somite and PSM interfaces as $\psi^s = 2\gamma A$, in which γ depicts surface energy density (surface tension). For somite boundary formation to initiate, the criterion of $\psi^e(d) \geq \psi^s$ needs to be satisfied, leading to a critical somite segment length $d = [4\gamma L / E(\varepsilon^*)^2]^{1/2}$. Thus, our theoretical model predicts a scaling relation between somite length d and PSM tissue length L as $d / \lambda \sim (L / \lambda)^{1/2}$, where $\lambda = 4\gamma / E(\varepsilon^*)^2$, and longer PSM tissues generate larger somites.

***In vivo* data extraction and model fitting**

To validate the theoretical scaling law that correlates somite length scale with PSM length scale, data about somite and PSM sizes in zebrafish[32,34], chicken[23,33], and mouse[10,31] embryo are extracted using software WebPlotDigitizer. For data in which PSM length and somite size are reported separately[31,34], they are combined by correlating the associated developmental stages. Also, for the 1D-rod assumption in our theoretical model to hold for the PSM tissue, it's necessary for the aspect ratio of the rod (or the PSM tissue) to be ≥ 5. Since the aspect ratio of somites *in vivo* is close to 1, in this work we only include data in which the PSM tissue length is at least five times of the nascent somite size.

***Young*'s modulus measurement by AFM**

AFM force-distance (F-D) measurements are conducted using a TT-AFM (AFMWorkshop, South Carolina, USA) and AFM probes with a 2-μm diameter bead tip and manufacturer-calibrated spring constant of 0.064 N m^{-1} (NovaScan, Iowa, USA). Measurements are taken at 1 mm spacing along the length of μSDM tissues, with μSDM tissue samples moved between locations using a manual Vernier micrometer. Approximately 10 F-D curves are collected at each location along μSDM tissues, and those curves with effective loading are used for analysis. QPD sensitivity is determined in fluid by collecting F-D curves on a stiff PDMS surface. F-D curves are analyzed using AtomicJ[52]. Before AFM measurements, the microfluidic devices are removed from coverslip substrates, and the tissues are incubated in Cell Recovery Solution (Corning) for 30 min to remove the gel and expose the tissues for subsequent AFM experiments. Furthermore, the tissues are imaged with bright field microscope before the AFM experiments, and the regions without rosette formation is designated as the PSM regime.

Calculation and comparison of surface energy density

Model fitting using *in vivo* and *in vitro* data of somite and PSM sizes allows us to determine the value of λ. To examine the physiological relevance of λ, we can compare the surface energy value γ deduced from λ with the measured value from zebrafish mesoderm. By linearly interpolating AFM measurements along the tissue length, the average *Young*'s modulus E of the PSM tissue is about 0.74 kPa (**Figure 5c**). The mean relative areal reduction of a forming somite recorded via live imaging is about 14.6% (**Figure 5d**). Since we only consider tissue shrinkage along the R-C axis of a forming somite, the associated eigen-strain can be approximated as $\varepsilon^* \approx -14.6\% / 2 = -7.3\%$. Given $\lambda = 4.41$ μm from data fitting in **Figure 5b**, we could determine the value of the surface energy density γ as 4.4 pN μm^{-1}.

In a recent work by Maître *et al.*[36], surface energy of zebrafish mesoderm is deconstructed into three parts, including cortical tension on cell-medium interface γ_{cm}, cortical tension on cell-cell interface γ_{cc}, and adhesion energy on cell-cell interface ω. The total energy associated with formation of somite boundary with area A can thus be written as $\psi^s = 2\gamma A = (2\gamma_{cm} - 2\gamma_{cc} - \omega)A = 2\gamma_{cm}(1 - \gamma_{cc} / \gamma_{cm} - \omega / 2\gamma_{cm})A$. Based on Maître *et al.*[36], for zebrafish mesoderm, γ_{cm} = 50 pN μm^{-1}, $\gamma_{cc} / \gamma_{cm} = 0.65$, and $\omega / 2\gamma_{cm} = -0.06$, which produces an effective γ = 20.5 pN μm^{-1}.

Mechanical stretching of μSDM

A custom-developed cell stretching device (CSD)[53] is employed to stretch μSDM tissues along their R-C axis direction (**Figure S5a**). Specifically, before the microfluidic device assembly, the PDMS micro-trench layer is attached to the CSD through plasma treatments on both the bottom surface of the PDMS micro-trench layer and the top surface of the CSD. The PDMS structural layer is then attached to the PDMS micro-trench layer, and μSDM tissue culture protocols proceed in the same way as previously described. On Day 5, the PDMS structural layer is removed from the device, and a mechanical loading with a 4-h period is applied to μSDM tissues inside micro-trenches for 24 h (**Figure S5c&d**). During this tissue stretching period, μSDM tissues are cultured in basal medium. To apply mechanical stretching of μSDM tissues, a trapezoidal voltage wave generated by a wave generator is converted to trapezoidal wave of vacuum pressure through a vacuum regulator (SMC Pneumatics, ITV0090). The trapezoidal wave of vacuum pressure is then loaded into the CSD to achieve uniaxial and periodical stretching of μSDM tissues inside micro-trenches (**Figure S5b**). On Day 6, μSDM tissues are fixed and processed for imaging. When fluorescence imaging is finished, the entire CSD device is placed under a brightfield microscope while the same vacuum pressure loading is applied. By measuring lengthening of micro-trenches, mechanical strain of μSDM tissues under different vacuum pressures are determined (**Figure S5d**).

Drug inhibition assays

For drug inhibition assays to block μSDM development, ADH-1 (0.2 mg mL^{-1}, AdooQ Bioscience), cytochalasin D (10 μM, Tocris), and Y27632 (10 μM, Tocris) are supplemented to both rostral and caudal reservoirs of the microfluidic device between Day 3 and 5. In blebbistatin assays, blebbistatin (10 μM, Sigma Aldrich) is supplemented to both reservoirs between Day 1 and 5. All μSDM tissue samples are fixed on Day 5. All small molecules used in this study are listed in **Key resources table**.

QUANTIFICATION AND STATISTICAL ANALYSIS

Statistical analyses are performed with OriginPro version 2023b. The statistical analysis method for each experiment is specified in the figure legend. For quantification, samples with air bubble trapped in microfluidic device during cell or gel loading are excluded. Samples with sub-optimal

cell deposition on Day 1 are also excluded. No similar platform has been previously reported, thus the criteria were established specifically for this platform. Samples were randomly allocated to control and different experimental groups. However, no particular randomization method was used in this work.

SUPPLEMENTARY VIDEOS

Supplementary Video 1. Spontaneous somite formation in μSDM, beginning rostrally and extending caudally, related to Figure 1 and S3. Time stamps indicate culture hours. Scale bar, 100 μm.

Supplementary Video 2. Cell dynamics in a forming somite in μSDM, related to Figure 2. Confocal imaging of a H2B reporter line shows cellular compaction and reorganization in a forming somite, leading to the formation of a somite with an epithelial appearance and a closely packed circumferential ring of columnar-shaped cells, elongated in the radial direction. Time stamps indicate culture hours. Scale bar, 100 μm.

Supplementary Video 3. Growth dynamics of a newly formed somite in μSDM, related to Figure 2 and S3. Confocal imaging of a newly formed somite shows a gradual increase of somite area, together with dynamic cell movements and division within the somite epithelial ring. Time stamps indicate culture hours. Scale bar, 100 μm.

Supplementary Video 4. Dynamics of somitocoel cells in μSDM, related to Figure 2 and S3. Confocal imaging of a formed somite showing centripetal movement of cells from the somite epithelium to the mesenchymal core of cells in the somitocoel. Time stamps indicate culture hours. Scale bar, 100 μm.

Supplementary Video 5. Oscillation and traveling waves of *HES7* signals in μSDM, related to Figure 4. Confocal imaging of a *HES7* reporter line shows oscillation and traveling waves of HES7 signals along the R-C axis of μSDM. Time stamps indicate culture hours. Scale bar, 200 μm.

1011

References for Main Text

Uncategorized References

1. Cooke, J., and Zeeman, E.C. (1976). A clock and wavefront model for control of the number of repeated structures during animal morphogenesis. J Theor Biol *58*, 455-476. 10.1016/s0022-5193(76)80131-2.
2. Dubrulle, J., McGrew, M.J., and Pourquié, O. (2001). FGF signaling controls somite boundary position and regulates segmentation clock control of spatiotemporal Hox gene activation. Cell *106*, 219-232.
3. Hubaud, A., and Pourquie, O. (2014). Signalling dynamics in vertebrate segmentation. Nat Rev Mol Cell Biol *15*, 709-721. 10.1038/nrm3891.
4. Simsek, M.F., Chandel, A.S., Saparov, D., Zinani, O.Q.H., Clason, N., and Ozbudak, E.M. (2023). Periodic inhibition of Erk activity drives sequential somite segmentation. Nature *613*, 153-159. 10.1038/s41586-022-05527-x.
5. Liu, Y., Xue, X., Sun, S., Kobayashi, N., Kim, Y.S., and Fu, J. (2024). Morphogenesis beyond in vivo. Nature Reviews Physics *6*, 28-44.
6. Simsek, M.F., and Ozbudak, E.M. (2018). Spatial Fold Change of FGF Signaling Encodes Positional Information for Segmental Determination in Zebrafish. Cell Rep *24*, 66-78 e68. 10.1016/j.celrep.2018.06.023.
7. Zheng, Y., Xue, X., Shao, Y., Wang, S., Esfahani, S.N., Li, Z., Muncie, J.M., Lakins, J.N., Weaver, V.M., Gumucio, D.L., and Fu, J. (2019). Controlled modelling of human epiblast and amnion development using stem cells. Nature *573*, 421-425. 10.1038/s41586-019-1535-2.
8. Moris, N., Anlas, K., van den Brink, S.C., Alemany, A., Schröder, J., Ghimire, S., Balayo, T., van Oudenaarden, A., and Martinez Arias, A. (2020). An in vitro model of early anteroposterior organization during human development. Nature *582*, 410-415. 10.1038/s41586-020-2383-9.
9. Warmflash, A., Sorre, B., Etoc, F., Siggia, E.D., and Brivanlou, A.H. (2014). A method to recapitulate early embryonic spatial patterning in human embryonic stem cells. Nat Methods *11*, 847-854. 10.1038/nmeth.3016.
10. Budjan, C., Liu, S., Ranga, A., Gayen, S., Pourquie, O., and Hormoz, S. (2022). Paraxial mesoderm organoids model development of human somites. Elife *11*. 10.7554/eLife.68925.
11. Sanaki-Matsumiya, M., Matsuda, M., Gritti, N., Nakaki, F., Sharpe, J., Trivedi, V., and Ebisuya, M. (2022). Periodic formation of epithelial somites from human pluripotent stem cells. Nat Commun *13*, 2325. 10.1038/s41467-022-29967-1.
12. Miao, Y., Djeffal, Y., De Simone, A., Zhu, K., Lee, J.G., Lu, Z., Silberfeld, A., Rao, J., Tarazona, O.A., Mongera, A., et al. (2022). Reconstruction and deconstruction of human somitogenesis in vitro. Nature. 10.1038/s41586-022-05655-4.
13. Yamanaka, Y., Hamidi, S., Yoshioka-Kobayashi, K., Munira, S., Sunadome, K., Zhang, Y., Kurokawa, Y., Ericsson, R., Mieda, A., Thompson, J.L., et al. (2022). Reconstituting human somitogenesis in vitro. Nature. 10.1038/s41586-022-05649-2.
14. Yaman, Y.I., and Ramanathan, S. (2023). Controlling human organoid symmetry breaking reveals signaling gradients drive segmentation clock waves. Cell *186*, 513-527 e519. 10.1016/j.cell.2022.12.042.
15. Xiong, F., Ma, W., Benazeraf, B., Mahadevan, L., and Pourquie, O. (2020). Mechanical Coupling Coordinates the Co-elongation of Axial and Paraxial Tissues in Avian Embryos. Dev Cell *55*, 354-366 e355. 10.1016/j.devcel.2020.08.007.
16. Regev, I., Guevorkian, K., Gupta, A., Pourquié, O., and Mahadevan, L. (2022). Rectified random cell motility as a mechanism for embryo elongation. Development *149*, dev199423.
17. Duband, J.L., Dufour, S., Hatta, K., Takeichi, M., Edelman, G.M., and Thiery, J.P. (1987). Adhesion molecules during somitogenesis in the avian embryo. J Cell Biol *104*, 1361-1374. 10.1083/jcb.104.5.1361.

18. Benazeraf, B., Francois, P., Baker, R.E., Denans, N., Little, C.D., and Pourquie, O. (2010). A random cell motility gradient downstream of FGF controls elongation of an amniote embryo. Nature *466*, 248-252. 10.1038/nature09151.
19. Akiyama, R., Masuda, M., Tsuge, S., Bessho, Y., and Matsui, T. (2014). An anterior limit of FGF/Erk signal activity marks the earliest future somite boundary in zebrafish. Development *141*, 1104-1109. 10.1242/dev.098905.
20. Zhai, J., Guo, J., Wan, H., Qi, L., Liu, L., Xiao, Z., Yan, L., Schmitz, D.A., Xu, Y., and Yu, D. (2022). Primate gastrulation and early organogenesis at single-cell resolution. Nature, 1-7.
21. Dequéant, M.L., and Pourquié, O. (2008). Segmental patterning of the vertebrate embryonic axis. Nat Rev Genet *9*, 370-382. 10.1038/nrg2320.
22. Diaz-Cuadros, M., Wagner, D.E., Budjan, C., Hubaud, A., Tarazona, O.A., Donelly, S., Michaut, A., Al Tanoury, Z., Yoshioka-Kobayashi, K., Niino, Y., et al. (2020). In vitro characterization of the human segmentation clock. Nature *580*, 113-118. 10.1038/s41586-019-1885-9.
23. Matsuda, M., Yamanaka, Y., Uemura, M., Osawa, M., Saito, M.K., Nagahashi, A., Nishio, M., Guo, L., Ikegawa, S., Sakurai, S., et al. (2020). Recapitulating the human segmentation clock with pluripotent stem cells. Nature *580*, 124-129. 10.1038/s41586-020-2144-9.
24. Chu, L.F., Mamott, D., Ni, Z., Bacher, R., Liu, C., Swanson, S., Kendziorski, C., Stewart, R., and Thomson, J.A. (2019). An In Vitro Human Segmentation Clock Model Derived from Embryonic Stem Cells. Cell Rep *28*, 2247-2255 e2245. 10.1016/j.celrep.2019.07.090.
25. Tsiairis, C.D., and Aulehla, A. (2016). Self-organization of embryonic genetic oscillators into spatiotemporal wave patterns. Cell *164*, 656-667.
26. Takahashi, Y., Sato, Y., Suetsugu, R., and Nakaya, Y. (2005). Mesenchymal-to-epithelial transition during somitic segmentation: a novel approach to studying the roles of Rho family GTPases in morphogenesis. Cells Tissues Organs *179*, 36-42. 10.1159/000084507.
27. Chaffer, C.L., Thompson, E.W., and Williams, E.D. (2007). Mesenchymal to epithelial transition in development and disease. Cells Tissues Organs *185*, 7-19. 10.1159/000101298.
28. Takahashi, Y., and Sato, Y. (2008). Somitogenesis as a model to study the formation of morphological boundaries and cell epithelialization. Development, growth & differentiation *50*, S149-S155.
29. Martins, G.G., Rifes, P., Amandio, R., Rodrigues, G., Palmeirim, I., and Thorsteinsdottir, S. (2009). Dynamic 3D cell rearrangements guided by a fibronectin matrix underlie somitogenesis. PLoS One *4*, e7429. 10.1371/journal.pone.0007429.
30. Beloussov, L.V., and Naumidi, II (1983). Cell contacts and rearrangements preceding somitogenesis in chick embryo. Cell Differ *12*, 191-204. 10.1016/0045-6039(83)90028-3.
31. Tam, P.P. (1981). The control of somitogenesis in mouse embryos. J Embryol Exp Morphol *65 Suppl*, 103-128.
32. Gomez, C., Ozbudak, E.M., Wunderlich, J., Baumann, D., Lewis, J., and Pourquie, O. (2008). Control of segment number in vertebrate embryos. Nature *454*, 335-339. 10.1038/nature07020.
33. Tenin, G., Wright, D., Ferjentsik, Z., Bone, R., McGrew, M.J., and Maroto, M. (2010). The chick somitogenesis oscillator is arrested before all paraxial mesoderm is segmented into somites. BMC developmental biology *10*, 1-12.
34. Thomson, L., Muresan, L., and Steventon, B. (2021). The zebrafish presomitic mesoderm elongates through compaction-extension. Cells & development *168*, 203748.
35. Nakatsu, T., Uwabe, C., and Shiota, K. (2000). Neural tube closure in humans initiates at multiple sites: evidence from human embryos and implications for the pathogenesis of neural tube defects. Anatomy and embryology *201*, 455-466.
36. Maitre, J.L., Berthoumieux, H., Krens, S.F., Salbreux, G., Julicher, F., Paluch, E., and Heisenberg, C.P. (2012). Adhesion functions in cell sorting by mechanically coupling the cortices of adhering cells. Science *338*, 253-256. 10.1126/science.1225399.

37. Nelemans, B.K.A., Schmitz, M., Tahir, H., Merks, R.M.H., and Smit, T.H. (2020). Somite Division and New Boundary Formation by Mechanical Strain. iScience *23*, 100976. 10.1016/j.isci.2020.100976.
38. Adhyapok, P., Piatkowska, A.M., Norman, M.J., Clendenon, S.G., Stern, C.D., Glazier, J.A., and Belmonte, J.M. (2021). A mechanical model of early somite segmentation. iScience *24*, 102317. 10.1016/j.isci.2021.102317.
39. Naganathan, S.R., and Oates, A.C. (2020). Patterning and mechanics of somite boundaries in zebrafish embryos. Semin Cell Dev Biol *107*, 170-178. 10.1016/j.semcdb.2020.04.014.
40. Burgess, R., Rawls, A., Brown, D., Bradley, A., and Olson, E.N. (1996). Requirement of the paraxis gene for somite formation and musculoskeletal patterning. Nature *384*, 570-573. 10.1038/384570a0.
41. Rowton, M., Ramos, P., Anderson, D.M., Rhee, J.M., Cunliffe, H.E., and Rawls, A. (2013). Regulation of mesenchymal-to-epithelial transition by PARAXIS during somitogenesis. Dev Dyn *242*, 1332-1344. 10.1002/dvdy.24033.
42. Mongera, A., Rowghanian, P., Gustafson, H.J., Shelton, E., Kealhofer, D.A., Carn, E.K., Serwane, F., Lucio, A.A., Giammona, J., and Campas, O. (2018). A fluid-to-solid jamming transition underlies vertebrate body axis elongation. Nature *561*, 401-405. 10.1038/s41586-018-0479-2.
43. Pourquie, O. (2001). Vertebrate somitogenesis. Annu Rev Cell Dev Biol *17*, 311-350. 10.1146/annurev.cellbio.17.1.311.
44. Lacoste, A., Berenshteyn, F., and Brivanlou, A.H. (2009). An efficient and reversible transposable system for gene delivery and lineage-specific differentiation in human embryonic stem cells. Cell Stem Cell *5*, 332-342. 10.1016/j.stem.2009.07.011.
45. Regot, S., Hughey, J.J., Bajar, B.T., Carrasco, S., and Covert, M.W. (2014). High-sensitivity measurements of multiple kinase activities in live single cells. Cell *157*, 1724-1734. 10.1016/j.cell.2014.04.039.
46. Oceguera-Yanez, F., Kim, S.-I., Matsumoto, T., Tan, G.W., Xiang, L., Hatani, T., Kondo, T., Ikeya, M., Yoshida, Y., and Inoue, H. (2016). Engineering the AAVS1 locus for consistent and scalable transgene expression in human iPSCs and their differentiated derivatives. Methods *101*, 43-55.
47. Serra, D., Mayr, U., Boni, A., Lukonin, I., Rempfler, M., Challet Meylan, L., Stadler, M.B., Strnad, P., Papasaikas, P., Vischi, D., et al. (2019). Self-organization and symmetry breaking in intestinal organoid development. Nature *569*, 66-72. 10.1038/s41586-019-1146-y.
48. Loh, K.M., Chen, A., Koh, P.W., Deng, T.Z., Sinha, R., Tsai, J.M., Barkal, A.A., Shen, K.Y., Jain, R., Morganti, R.M., et al. (2016). Mapping the Pairwise Choices Leading from Pluripotency to Human Bone, Heart, and Other Mesoderm Cell Types. Cell *166*, 451-467. 10.1016/j.cell.2016.06.011.
49. Butler, A., Hoffman, P., Smibert, P., Papalexi, E., and Satija, R. (2018). Integrating single-cell transcriptomic data across different conditions, technologies, and species. Nat Biotechnol *36*, 411-420. 10.1038/nbt.4096.
50. Gao, M., Qiao, C., and Huang, Y. (2022). UniTVelo: temporally unified RNA velocity reinforces single-cell trajectory inference. Nat Commun *13*, 6586. 10.1038/s41467-022-34188-7.
51. Street, K., Risso, D., Fletcher, R.B., Das, D., Ngai, J., Yosef, N., Purdom, E., and Dudoit, S. (2018). Slingshot: cell lineage and pseudotime inference for single-cell transcriptomics. BMC Genomics *19*, 477. 10.1186/s12864-018-4772-0.
52. Hermanowicz, P., Sarna, M., Burda, K., and Gabryś, H. (2014). AtomicJ: an open source software for analysis of force curves. Review of Scientific Instruments *85*, 063703.
53. Shao, Y., Mann, J.M., Chen, W., and Fu, J. (2014). Global architecture of the F-actin cytoskeleton regulates cell shape-dependent endothelial mechanotransduction. Integr Biol (Camb) *6*, 300-311. 10.1039/c3ib40223a.

1160

CellPress

KEY RESOURCES TABLE

The table highlights the reagents, genetically modified organisms and strains, cell lines, software, instrumentation, and source data **essential** to reproduce results presented in the manuscript. Depending on the nature of the study, this may include standard laboratory materials (i.e., food chow for metabolism studies, support material for catalysis studies), but the table is **not** meant to be a comprehensive list of all materials and resources used (e.g., essential chemicals such as standard solvents, SDS, sucrose, or standard culture media do not need to be listed in the table). **Items in the table must also be reported in the method details section within the context of their use.** To maximize readability, the number of **oligonucleotides and RNA sequences** that may be listed in the table is restricted to no more than 10 each. If there are more than 10 oligonucleotides or RNA sequences to report, please provide this information as a supplementary document and reference the file (e.g., See Table S1 for XX) in the key resources table.

Please note that ALL references cited in the key resources table must be included in the main references list. Please report the information as follows:

- **REAGENT or RESOURCE:** Provide the full descriptive name of the item so that it can be identified and linked with its description in the manuscript (e.g., provide version number for software, host source for antibody, strain name). In the experimental models section (applicable only to experimental life science studies), please include all models used in the paper and describe each line/strain as: model organism: name used for strain/line in paper: genotype. (i.e., Mouse: $OXTR^{fl/fl}$: B6.129(SJL)-$Oxtr^{tm1.1Wsy/J}$). In the biological samples section (applicable only to experimental life science studies), please list all samples obtained from commercial sources or biological repositories. Please note that software mentioned in the methods details or data and code availability section needs to also be included in the table. See the sample tables at the end of this document for examples of how to report reagents.

- **SOURCE:** Report the company, manufacturer, or individual that provided the item or where the item can be obtained (e.g., stock center or repository). For materials distributed by Addgene, please cite the article describing the plasmid and include “Addgene” as part of the identifier. If an item is from another lab, please include the name of the principal investigator and a citation if it has been previously published. If the material is being reported for the first time in the current paper, please indicate as “this paper.” For software, please provide the company name if it is commercially available or cite the paper in which it has been initially described.

- **IDENTIFIER:** Include catalog numbers (entered in the column as “Cat#” followed by the number, e.g., Cat#3879S). Where available, please include unique entities such as RRIDs, Model Organism Database numbers, accession numbers, and PDB, CAS, or CCDC IDs. For antibodies, if applicable and available, please also include the lot number or clone identity. For software or data resources, please include the URL where the resource can be downloaded. Please ensure accuracy of the identifiers, as they are essential for generation of hyperlinks to external sources when available. Please see the Elsevier list of data repositories with automated bidirectional linking for details. When listing more than one identifier for the same item, use semicolons to separate them (e.g., Cat#3879S; RRID: AB_2255011). If an identifier is not available, please enter “N/A” in the column.
    - ***A NOTE ABOUT RRIDs:*** We highly recommend using RRIDs as the identifier (in particular for antibodies and organisms but also for software tools and databases). For more details on how to obtain or generate an RRID for existing or newly generated resources, please visit the RII or search for RRIDs.

Please use the empty table that follows to organize the information in the sections defined by the subheading, skipping sections not relevant to your study. Please do not add subheadings. To add a row, place the cursor at the end of the row above where you would like to add the row, just outside the right border of the table. Then press the ENTER key to add the row. Please delete empty rows. Each entry must be on a separate row; do not list multiple items in a single table cell. Please see the sample tables at the end of this document for relevant examples in the life and physical sciences of how reagents and instrumentation should be cited.

TABLE FOR AUTHOR TO COMPLETE

Please upload the completed table as a separate document. ***Please do not add subheadings to the key resources table.*** *If you wish to make an entry that does not fall into one of the subheadings below, please contact your handling editor.* ***Any subheadings not relevant to your study can be skipped.*** *(**NOTE:** References within the KRT should be in numbered style rather than Harvard.)*

Key resources table

REAGENT or RESOURCE	SOURCE	IDENTIFIER
Antibodies		
PAX3	DSHB	N/A
TBX6	R&D Systems	AF4744-SP
Fibronectin	BD Biosciences	610077
ZO1	Thermo Fisher Scientific	33-9100
HOXC9	Abcam	ab50839
HOXC10	Abcam	ab153904
Chemicals, peptides, and recombinant proteins		
CHIR99021	STEMCELL Technologies	100-1042
LDN193189	STEMCELL Technologies	72147
Y27632	Tocris	1254
PD 173074	Tocris	30-441-0
Retinoic acid	STEMCELL Technologies	72262
FGF8	PEPROTECH	100-25
ADH-1	AdooQ Bioscience	A13689
Cytochalasin D	Tocris	1233
Blebbistatin	Sigma Aldrich	B0560-1MG
Janelia Fluor® HaloTag® Ligands	Promega	GA1120
Deposited data		
Raw and analyzed scRNA-seq data	This study	GEO: GSE236668
Differentially expressed genes, compared human and monkey markers, and used oligonucleotides (Mendeley Table S1-3)	This study	DOI: doi.org/10.17632/z4jncwx9ks.2
Experimental models: Cell lines		
Human: hESC H9	WiCell	WA09
Human: hESC H1	WiCell	WA01
Human: NCRM1 hiPSC	Diaz-Cuadros et al.	N/A
Oligonucleotides		
All oligonucleotides used in this study are deposited on Mendeley (Mendeley Table S3)	This study	DOI: doi.org/10.17632/z4jncwx9ks.2
Software and algorithms		
Matlab R2011a	N/A	https://www.mathworks.com/products/matlab.html

ImageJ 1.53t	N/A	https://imagej.net/software/fiji/downloads
Rstudio 2022.07.2	N/A	https://posit.co/products/open-source/rstudio/
Seurat 4.2.0	N/A	https://satijalab.org/seurat/articles/install_v5
Excel 2016	N/A	https://www.microsoft.com/en-us/microsoft-365/excel

Figure 1

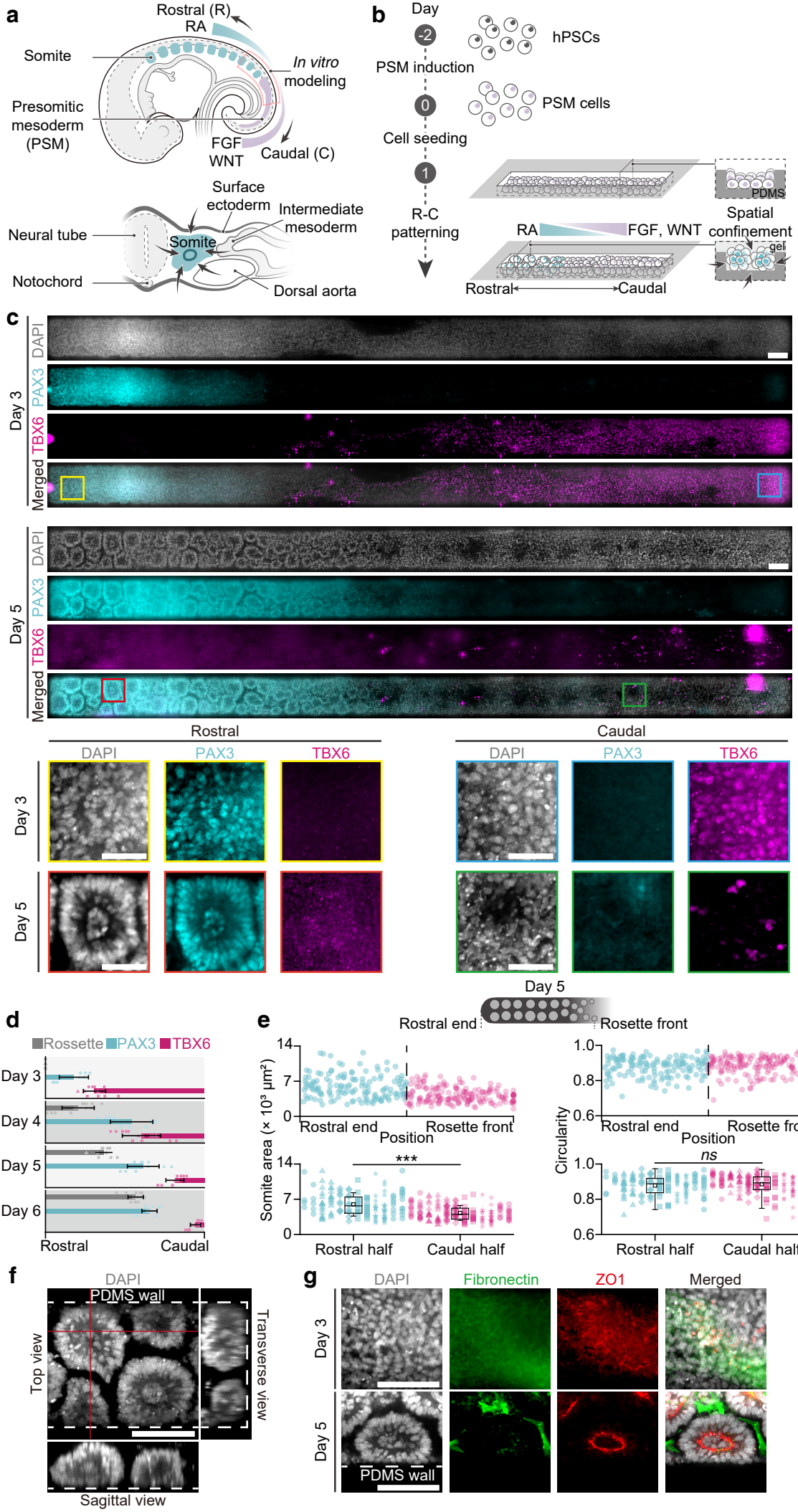
a
Rostral (R)
RA
Somite
In vitro modeling
Presomitic mesoderm (PSM)
FGF
WNT
Caudal (C)
Surface ectoderm
Intermediate mesoderm
Neural tube
Somite
Notochord
Dorsal aorta
b
Day
-2
hPSCs
PSM induction
0
PSM cells
Cell seeding
1
R-C patterning
PDMS
Spatial confinement
RA
FGF, WNT
gel
Rostral
Caudal
c
Day 3
Day 5
DAPI
PAX3
TBX6
Merged
Rostral
Caudal
d
Rossette
PAX3
TBX6
Day 3
Day 4
Day 5
Day 6
Rostral
Caudal
e
Day 5
Rostral end
Rosette front
Somite area (× 10³ µm²)
Position
Rostral half
Caudal half
***
Circularity
ns
f
DAPI
PDMS wall
Top view
Transverse view
Sagittal view
g
DAPI
Fibronectin
ZO1
Merged
Day 3
Day 5
PDMS wall

Figure 2

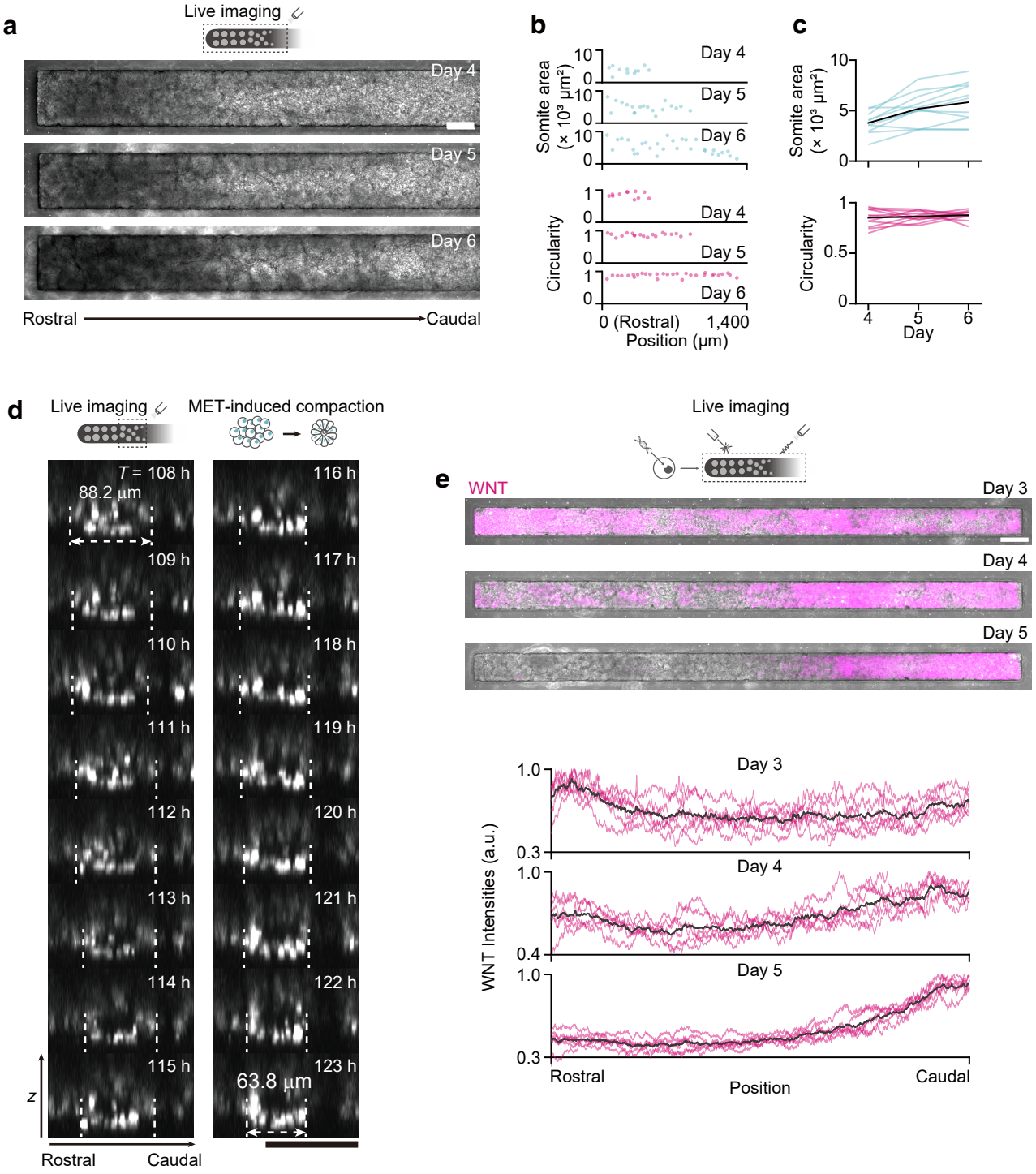
a
Live imaging
Day 4
Day 5
Day 6
Rostral
Caudal
b
Somite area (× 10³ μm²)
Day 4
Day 5
Day 6
Circularity
0 (Rostral)
1,400
Position (μm)
c
Somite area (× 10³ μm²)
Circularity
Day
d
Live imaging
MET-induced compaction
T = 108 h
88.2 μm
109 h
110 h
111 h
112 h
113 h
114 h
115 h
116 h
117 h
118 h
119 h
120 h
121 h
122 h
123 h
63.8 μm
z
Rostral
Caudal
e
Live imaging
WNT
Day 3
Day 4
Day 5
WNT Intensities (a.u.)
Rostral
Position
Caudal

Figure 3

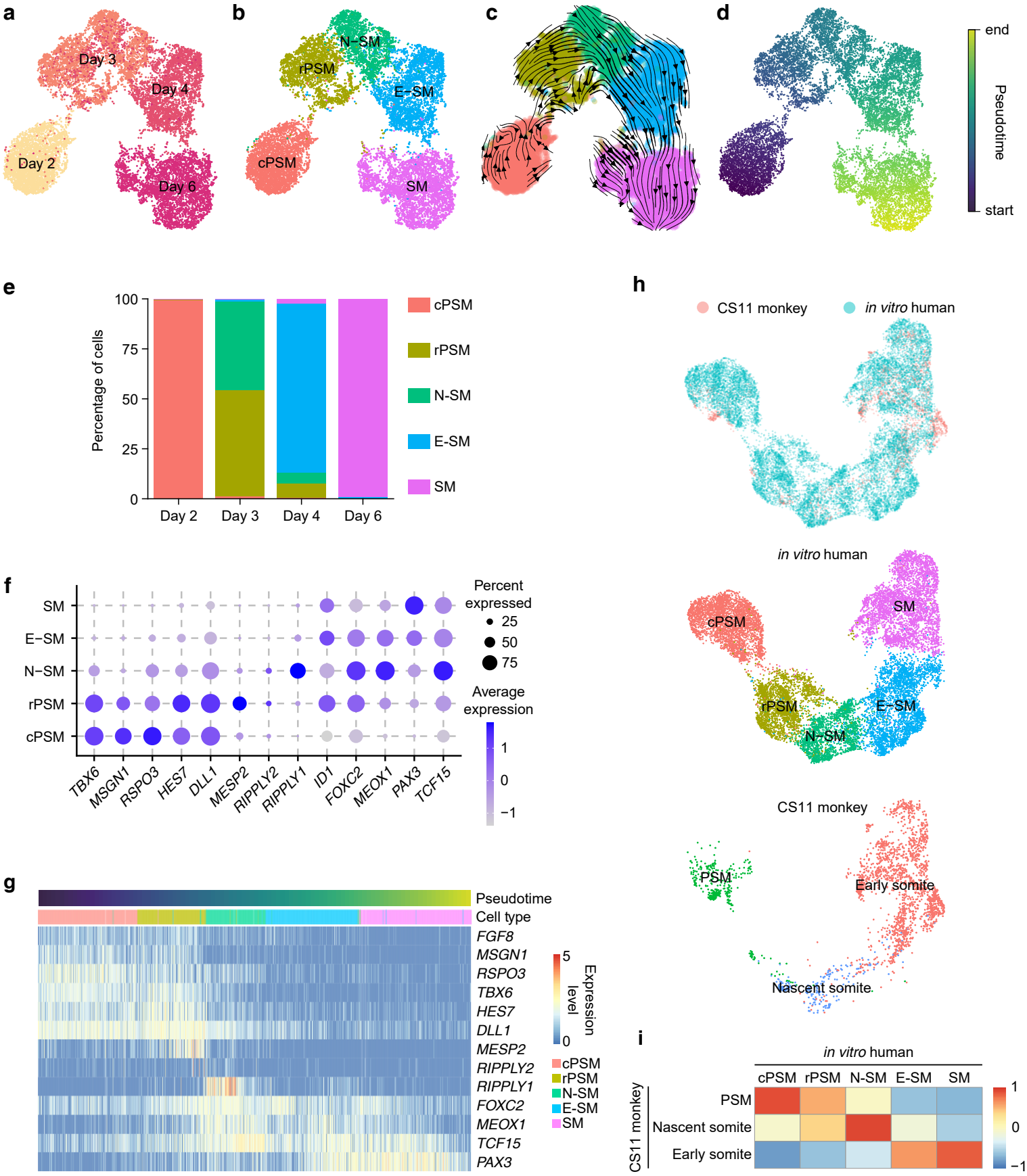
a
Day 3
Day 4
Day 2
Day 6
b
N−SM
rPSM
E−SM
cPSM
SM
c
d
end
Pseudotime
start
e
Percentage of cells
100
75
50
25
0
Day 2
Day 3
Day 4
Day 6
cPSM
rPSM
N-SM
E-SM
SM
f
SM
E−SM
N−SM
rPSM
cPSM
TBX6
MSGN1
RSPO3
HES7
DLL1
MESP2
RIPPLY2
RIPPLY1
ID1
FOXC2
MEOX1
PAX3
TCF15
Percent expressed
25
50
75
Average expression
1
0
−1
g
Pseudotime
Cell type
FGF8
MSGN1
RSPO3
TBX6
HES7
DLL1
MESP2
RIPPLY2
RIPPLY1
FOXC2
MEOX1
TCF15
PAX3
5
Expression level
0
cPSM
rPSM
N-SM
E-SM
SM
h
CS11 monkey
in vitro human
in vitro human
cPSM
SM
rPSM
E−SM
N−SM
CS11 monkey
PSM
Early somite
Nascent somite
i
in vitro human
cPSM
rPSM
N-SM
E-SM
SM
CS11 monkey
PSM
Nascent somite
Early somite
1
0
−1

Figure 4

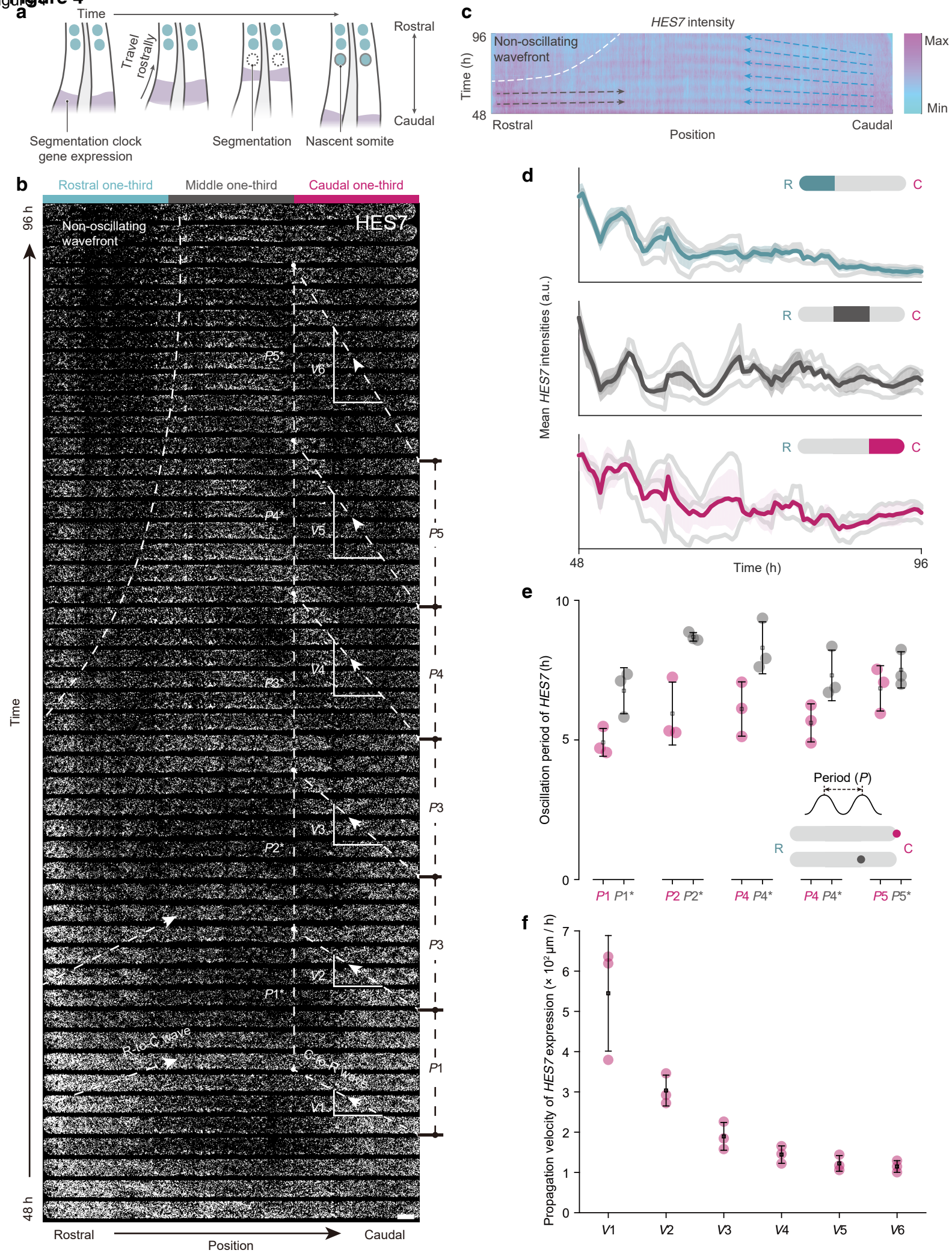
a
Time
Travel rostrally
Rostral
Caudal
Segmentation clock gene expression
Segmentation
Nascent somite
b
Rostral one-third
Middle one-third
Caudal one-third
96 h
48 h
Time
Non-oscillating wavefront
HES7
P5*
V6
P4*
V5
P3*
V4
P2*
V3
V2
P1*
V1
R-to-C wave
C-to-R wave
P5
P4
P3
P3
P1
Rostral
Caudal
Position
c
HES7 intensity
96
48
Time (h)
Non-oscillating wavefront
Max
Min
Rostral
Caudal
Position
d
Mean HES7 intensities (a.u.)
R
C
48
96
Time (h)
e
Oscillation period of HES7 (h)
10
5
0
Period (P)
P1 P1*
P2 P2*
P4 P4*
P4 P4*
P5 P5*
f
Propagation velocity of HES7 expression (× 10² μm / h)
7
6
5
4
3
2
1
0
V1
V2
V3
V4
V5
V6

Figure 5

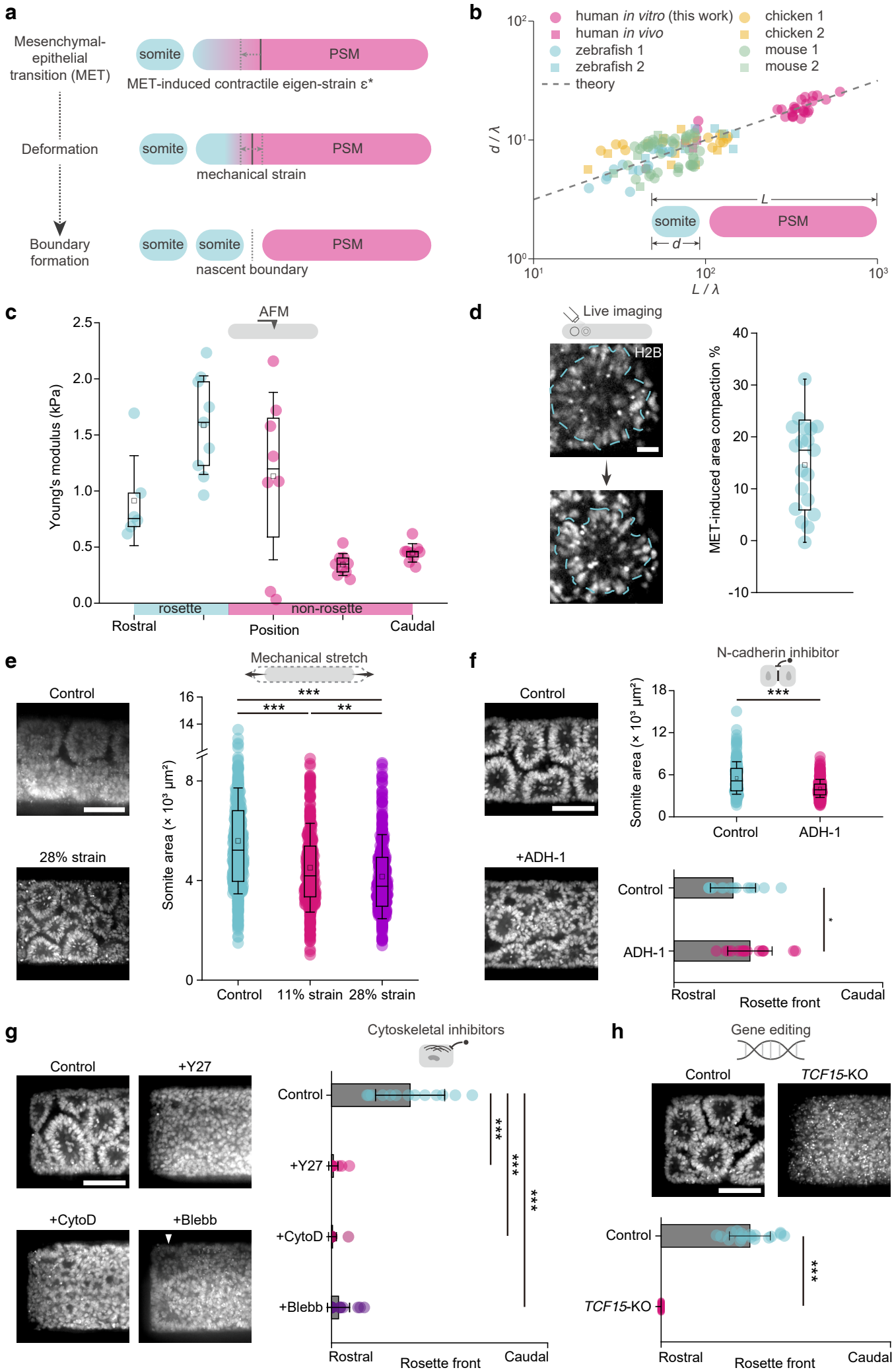
a
Mesenchymal-epithelial transition (MET)
somite
PSM
MET-induced contractile eigen-strain ε*
Deformation
mechanical strain
Boundary formation
nascent boundary
b
human in vitro (this work)
human in vivo
zebrafish 1
zebrafish 2
chicken 1
chicken 2
mouse 1
mouse 2
theory
d / λ
L / λ
L
d
c
AFM
Young's modulus (kPa)
rosette
non-rosette
Rostral
Position
Caudal
d
Live imaging
H2B
MET-induced area compaction %
e
Control
28% strain
Mechanical stretch
Somite area (× 10³ μm²)
Control
11% strain
28% strain
f
Control
+ADH-1
N-cadherin inhibitor
Somite area (× 10³ μm²)
ADH-1
Rostral
Rosette front
Caudal
g
Control
+Y27
+CytoD
+Blebb
Cytoskeletal inhibitors
h
Gene editing
Control
TCF15-KO
Rostral
Rosette front
Caudal

Supplementary Figure 1

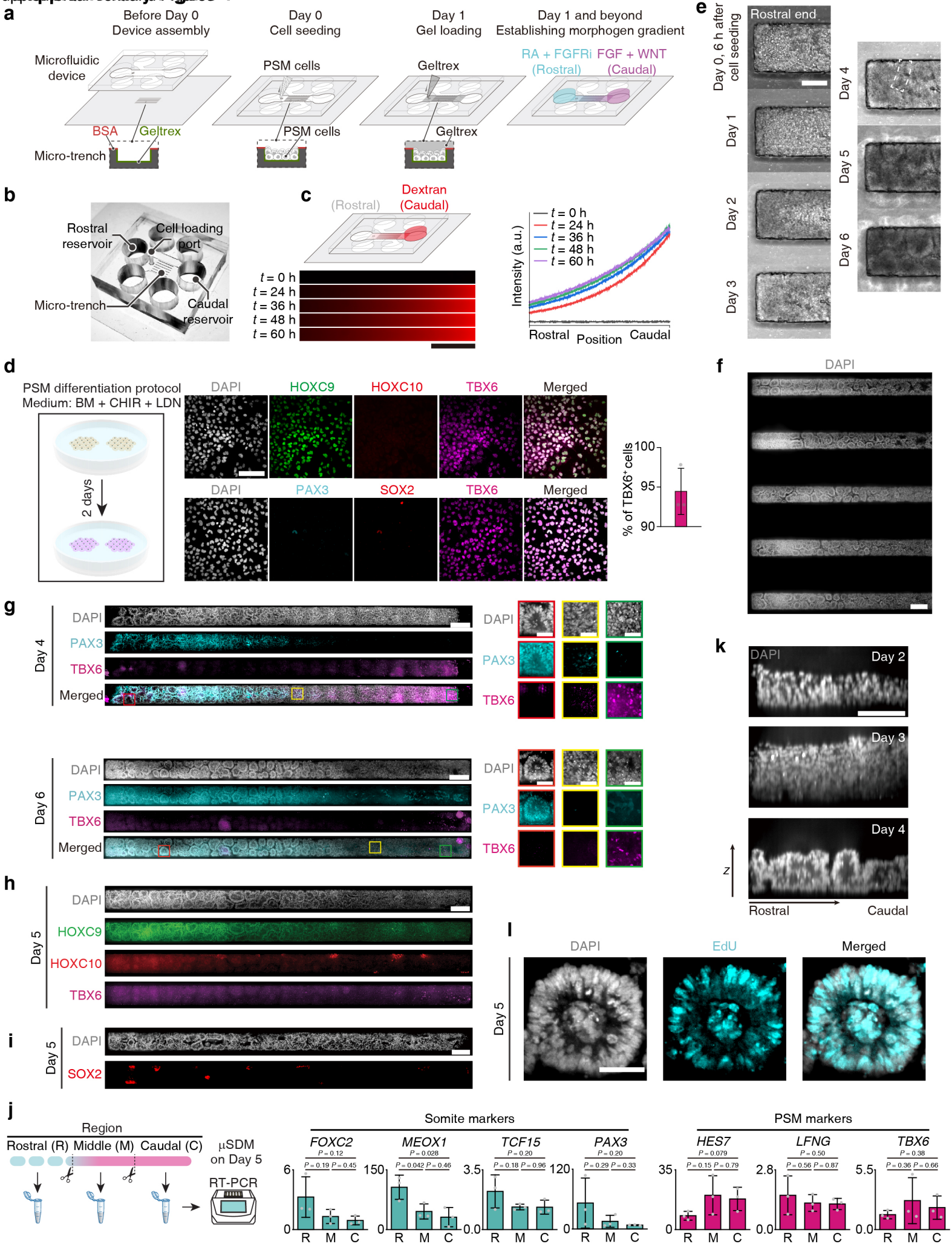

Figure S1. Culture protocol and characterization of microfluidic somite development model (μSDM), related to Figures 1. **a**, Schematics of μSDM device fabrication and its culture protocol. See **Methods** for μSDM design considerations. **b**, Image showing an assembled μSDM device. **c**, (left, top) Characterization of molecular diffusion in μSDM device by supplementing fluorescent dextran to the caudal reservoir. (left, bottom) Representative stitched micrographs showing diffusion of fluorescent dextran inside the microfluidic channel in the caudal (C)-to-rostral (R) direction over time. (right) Plot of fluorescence intensity along the microfluidic channel length over time as indicated. Fluorescence intensity is averaged across the microfluidic channel width. A stabilized fluorescent gradient pattern was established in the microfluidic channel within about 36 h. **d**, Derivation of presomitic mesoderm (PSM) cells from hPSCs. (left) Schematics of PSM differentiation protocol. (middle) Representative immunostaining images showing PSM cells stained positive for HOXC9 and TBX6, but negative for HOXC10, PAX3 or SOX2. (right) Bar plot showing percentage of $TBX6^+$ PSM cells. Data are plotted as the mean ± s.d., with $n = 3$. **e**, Brightfield live imaging to examine cellular dynamics and spontaneous somite formation at the rostral end of a micro-trench over time. A forming boundary on Day 4 is marked by a white box. **f**, Representative stitched confocal image showing consistent rosette propagation from rostral ends of a micro-trench array. **g**, Representative stitched confocal micrographs showing μSDM on Day 4 and Day 6 stained for PAX3 and TBX6. Cell nuclei were counterstained with DAPI. Zoom-in views of three boxed regions are shown at the bottom. **h**, Representative stitched confocal micrographs showing μSDM on Day 5 stained for HOXC9, HOXC10 and TBX6. Cell nuclei were counterstained with DAPI. **i**, Representative stitched confocal micrographs showing μSDM on Day 5 stained for SOX2. Cell nuclei were counterstained with DAPI. **j**, (left) Schematic showing dissection of μSDM on Day 5 using a surgical scissor into rostral (R), middle (M), and caudal (C) tissue segments of equal lengths for downstream RT-qPCR analysis, and (right) bar plots showing normalized expression of different somite and PSM markers as indicated, as a function of the three segments of Day 5 μSDM. $n = 3$, with $n_{\mu SDM} = 6$. P values calculated from two-sample t-tests are indicated. **k**, Representative sagittal views for confocal z stack images of the rostral ends of μSDM between day 2 and day 4. **l**, Representative confocal micrographs showing somite on Day 5 with EdU labeling. Cell nuclei were counterstained with DAPI. Scale bars: 1

mm (**c**); 100 µm (**d** & **e**); 200 µm (**f**); 200 µm for full-tissue images and 50 µm for zoom-in images (**g**); 200 µm (**h** & **i**); 100 µm (**k**); 50 µm (**l**).

Supplementary Figure 2

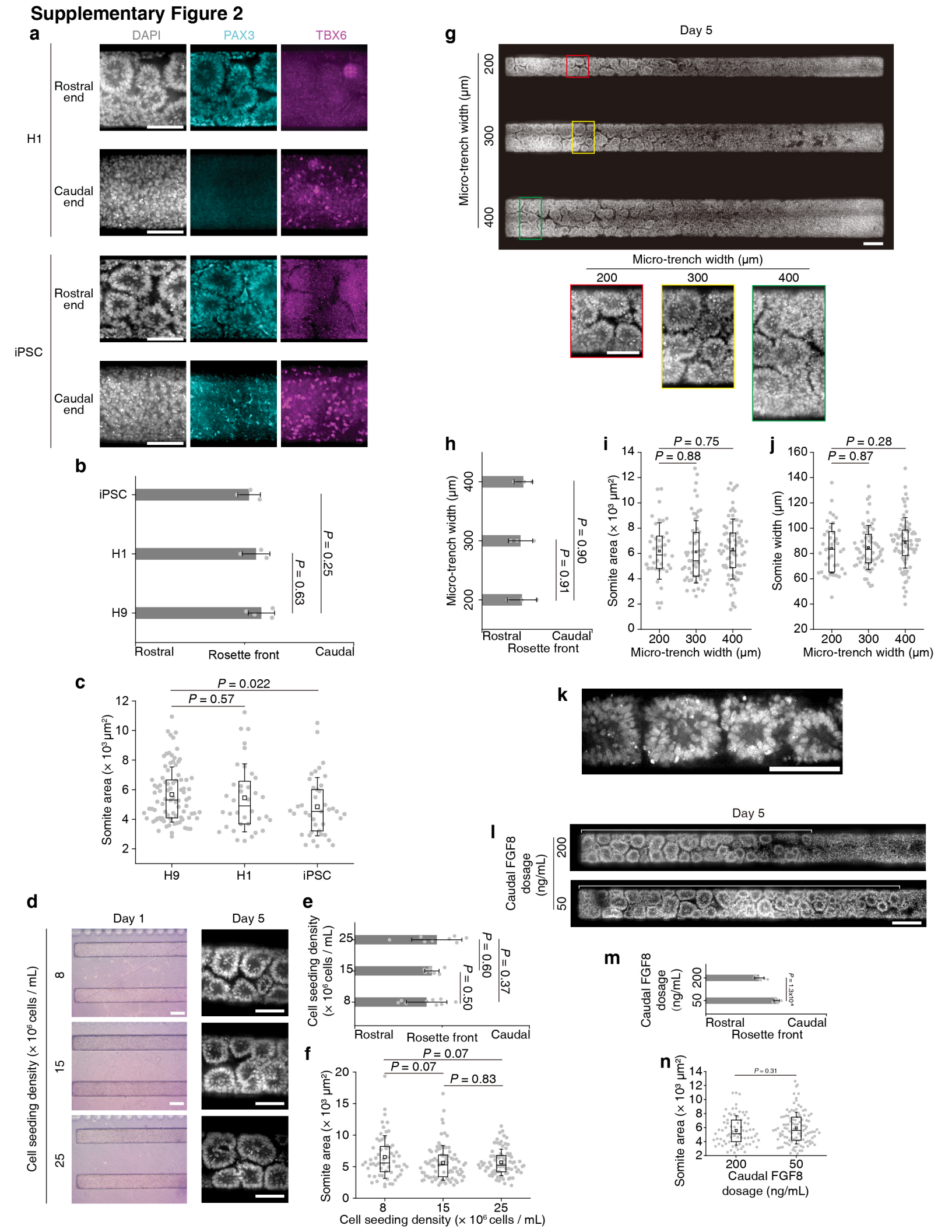

Figure S2. Development of μSDM using different conditions and cell/tissue dynamics during somite formation revealed by live imaging, related to Figure 1. **a**, Representative confocal micrographs showing rostral and caudal ends of μSDM derived from H1 hESC and hiPSC lines on Day 5 stained for PAX3 and TBX6 as indicated. Cell nuclei were counterstained with DAPI. **b**, Bar plot showing spatial regimes of somite formation in μSDM on Day 5 as a function of H9 and H1 hESC lines and a hiPSC line. For H9, $n_{\mu SDM} = 4$; for H1 and hiPSC, $n_{\mu SDM} = 3$. Data are plotted as the mean ± s.d. **c**, Areas of individual somites in μSDM on Day 5 as a function of H9 and H1 hESC lines and a hiPSC line. For H9, $n_{somite} = 86$; for H1, $n_{somite} = 36$; for hiPSC, $n_{somite} = 41$. Boxes and bars indicate interquartile ranges and median values, respectively, and squares and error bars indicate the mean ± s.d. *P* values calculated from two-sample *t*-tests are indicated. **d**, (left) Representative brightfield micrographs showing micro-trenches filled with hPSCs on Day 1 under different cell seeding density conditions as indicated. (right) Representative confocal micrographs showing individual somites in μSDM on Day 5 stained with DAPI under different cell seeding density conditions as indicated. **e**, Bar plot showing spatial regimes of somite formation in μSDM on Day 5 as a function of cell seeding density. For 8×10^6 cells / mL, $n_{\mu SDM} = 9$; for 15×10^6 cells / mL, $n_{\mu SDM} = 8$; For 25×10^6 cells / mL, $n_{\mu SDM} = 8$. Data are plotted as the mean ± s.d. *P* values calculated from two-sample *t*-tests are indicated. **f**, Areas of individual somites in μSDM on Day 5 as a function of cell seeding density. For all conditions, $n_{\mu SDM} = 4$. For 8×10^6 cells / mL, $n_{somite} = 80$; for 15×10^6 cells / mL, $n_{somite} = 115$; For 25×10^6 cells / mL, $n_{somite} = 106$. Boxes and bars indicate interquartile ranges and median values, respectively, and squares and error bars indicate the mean ± s.d. *P* values calculated from two-sample *t*-tests are indicated. **g**, Representative stitched confocal micrographs showing μSDM on Day 5 developed in micro-trenches with different widths stained with DAPI as indicated. Zoom-in views of boxed regions are shown on the bottom. **h**, Bar plot showing spatial patterns of somite formation in μSDM on Day 5 as a function of micro-trench width. For all conditions, $n_{\mu SDM} = 3$. Data are plotted as the mean ± s.d. *P* values calculated from two-sample *t*-tests are indicated. **i**, **j**, Areas (**i**) and lateral width (**j**) of individual somites in μSDM on Day 5 as a function of micro-trench width. For all conditions, $n_{\mu SDM} = 3$. For micro-trench width of 200 μm, $n_{somite} = 39$; for micro-trench width of 300 μm, $n_{somite} = 60$; for micro-trench width of 400 μm, $n_{somite} = 74$. Boxes and bars indicate interquartile ranges and median values, respectively, and squares and error bars indicate the mean ± s.d. *P* values calculated

from two-sample *t*-tests are indicated. **k**, Representative confocal micrograph showing a linear sequence of somites in the rostral region of μSDM developed in 100 μm-wide micro-trenches stained with DAPI. **l**, Representative stitched confocal micrographs showing μSDM on Day 5 stained with DAPI. Different FGF8 conditions were used for μSDM development as indicated. Somite formation regions are marked by while bars. Scale bar, 200 μm. **m**, Bar plot showing spatial regimes of somite formation in μSDM on Day 5 as a function of FGF8 concentration in the caudal reservoir. $n_{\mu SDM} = 7$ (50 ng/mL) and $n_{\mu SDM} = 8$ (200 ng/mL). Data are plotted as the mean ± s.d. *P* values calculated from two-sample *t*-tests are indicated. **n**, Areas of individual somites in μSDM on Day 5 as a function of FGF8 dose in the caudal reservoir. For both conditions, $n_{\mu SDM} = 3$. For FGF8 dose of 50 ng/mL, $n_{somite} = 105$; for FGF8 dose of 200 ng/mL, $n_{somite} = 73$. Boxes and bars indicate interquartile ranges and median values, respectively, and squares and error bars indicate the mean ± s.d. *P* values calculated from two-sample *t*-tests are indicated. Scale bars, 100 μm (**a** & **k**); 200 μm (brightfield images) and 100 μm (staining images) (**d**); 200 μm (full-tissue) and 100 μm (zoom-in) (**g**); 200 μm (**l**).

Supplementary Figure 3

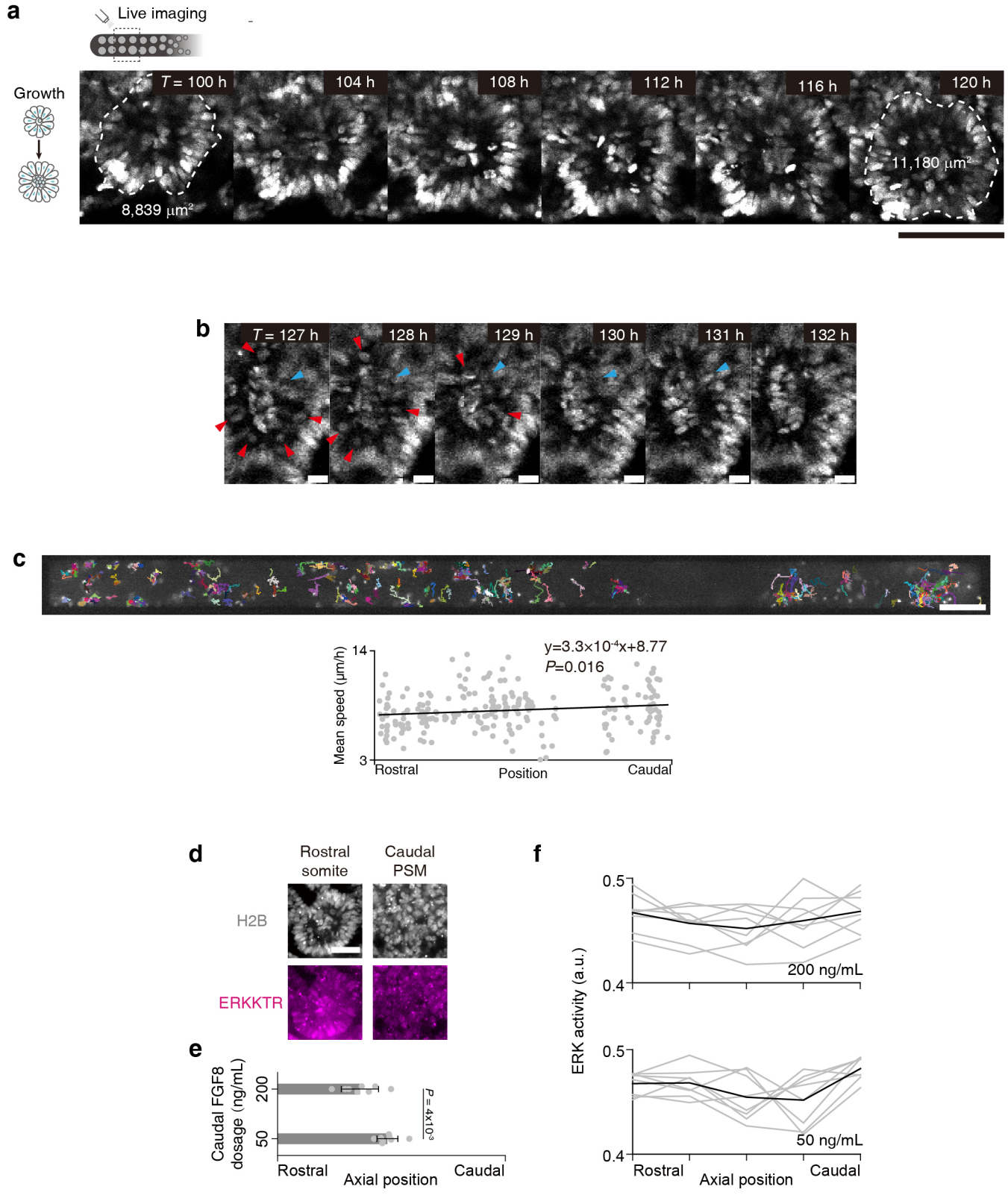

Figure S3. Cell/tissue dynamics during somite formation revealed by live imaging, related to Figure 2. **a**, Confocal imaging of growth dynamics of a newly formed somite, showing dynamic cell movements and division within the somite epithelial ring. **b**, Confocal imaging of a formed somite showing centripetal movement of cells from the somite epithelium to the mesenchymal core of cells in the somitocoel. Red triangles mark movements of individual cells whereas blue triangles mark movements of cell clusters from the somite epithelium towards the somitocoel. **c**, (top) Epifluorescence imaging revealing the cell migration in μSDM developed from H9 cells spiked with diluted H2B-GFP H9 reporter cells, whose trajectories between Day 3 and Day 4 are marked by colored lines. (bottom) A linear fitting between mean migration speeds of H2B-GFP reporter cells and their locations at the beginning of the tracking. Each data point is from a single H2B positive cell. The parameters and the *P*-value calculated from the fitting are indicated. **d**, Representative confocal micrographs showing μSDM developed from a H2B-mCherry;ERKKTR-Halo iPSC reporter on Day 5. **e**, Bar plot showing spatial regimes of somite formation in ERKKTR reporter-based μSDM on Day 5 as a function of FGF8 concentration in the caudal reservoir. Data are plotted as the mean ± s.d. *P* values calculated from two-sample *t*-tests are indicated. **f**, Intensities of ERK activities in μSDM on Day 5 under different FGF8 concentrations in the caudal reservoir as indicated. Each light grey line represents an individual μSDM while black line shows the mean value. For data in **e** and **f**, $n_{\mu SDM} = 8$. Scale bars, 100 μm (**a**); 10 μm (**b**); 200 μm (**c**); and 50 μm (**d**).

Supplementary Figure 4

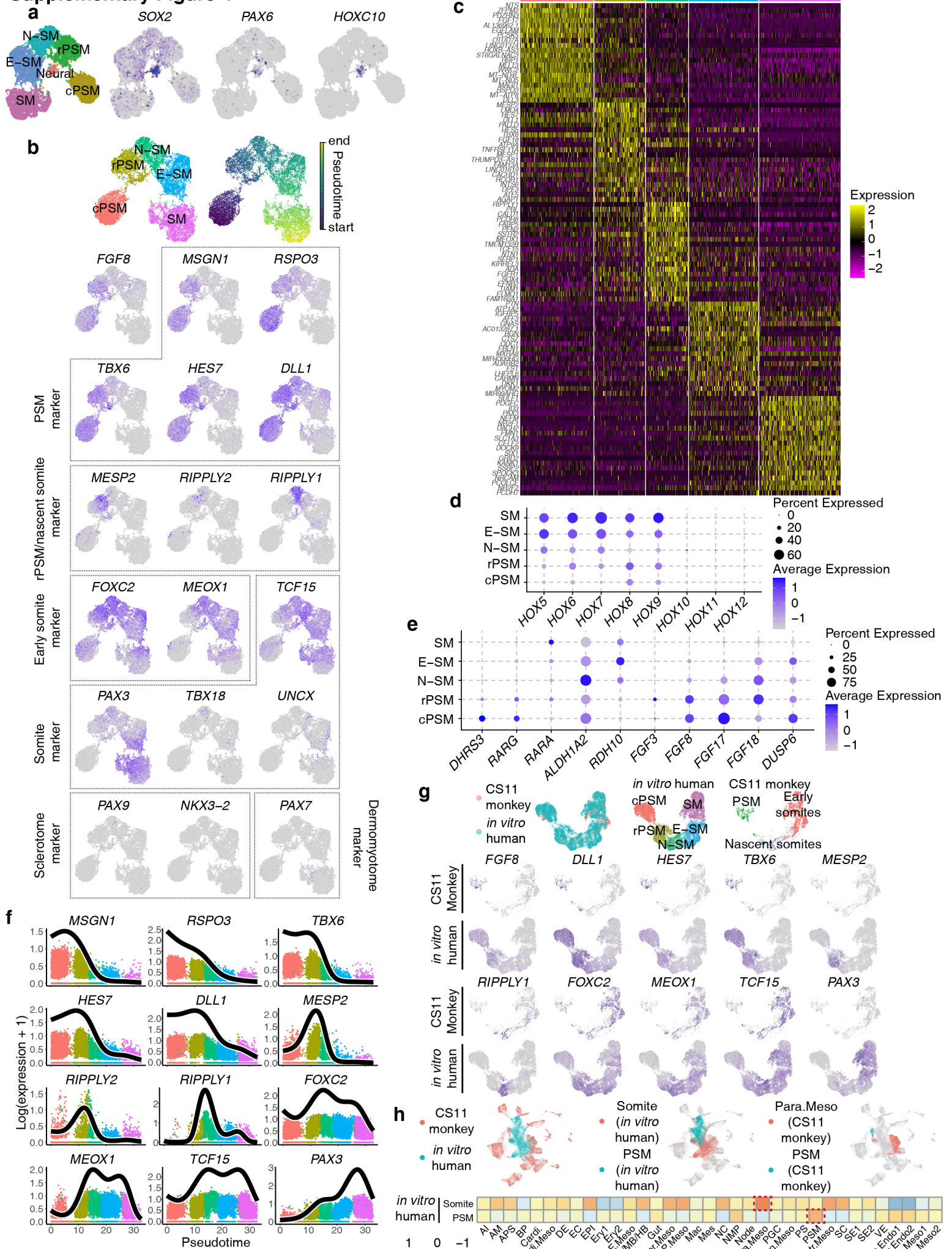

Figure S4. scRNA-seq analysis of marker expression in μSDM, related to Figure 3. a, (left) UMAP embedding of integrated single-cell transcriptome dataset of μSDM on Day 2, Day 3, Day 4 and Day 6 with the neural lineage included, color-coded by cell identity annotation and (right) Feature plots showing expression patterns of key neural marker genes, *SOX*2 and *PAX*6, and axial identity gene, *HOXC*10. **b**, (top) UMAP embedding of integrated single-cell transcriptome dataset of μSDM on Day 2, Day 3, Day 4 and Day 6, color-coded by cell identity annotation (top left) and pseudo-time (top right). (bottom) Feature plots showing expression patterns of key genes involved in the somitogenesis, including markers of the PSM, somite, sclerotome and dermomyotome as indicated. **c**, Heatmap of top-20 differentially expressed genes among all identified mesodermal lineages in μSDM. The color bar above the heat map indicates cell identity. **d & e**, Dot plots showing expression of *HOX*5-12 and RA and FGF signaling-related genes across different cell clusters in μSDM. Dot sizes and colors indicate proportions of cells expressing corresponding genes and their averaged scaled values of log-transformed expression, respectively. **f**, Expression levels of selected genes are fitted to principal curves to show general trends of their regulation. **g.** (top left) UMAP projection of integrated scRNA-seq dataset from μSDM and somitogenesis-related cells from a CS11 monkey embryo[1]. (top middle and right) UMAP projections of datasets from μSDM and the CS11 monkey embryo, separated from the integrated UMAP plot, with cell identity annotations indicated. (bottom) Feature plots comparing expression patterns of key PSM and somite markers in μSDM and the CS11 monkey embryo as indicated. cPSM, caudal PSM; rPSM, rostral PSM; N-SM, nascent somite; E-SM, early somite; SM, somite. **h**, (top left) UMAP projection of integrated scRNA-seq dataset from μSDM and all cell lineages from a CS11 monkey embryo[1]. (top middle and right) UMAP projections of datasets from μSDM and the full CS11 monkey embryo with PSM and somite/paraxial mesoderm identity annotations indicated. (bottom) Pearson's correlation analysis of μSDM PSM and somite cell clusters with all cell clusters in the CS11 monkey embryo. Highest correlations identified for the PSM and somite lineages are marked by red squares.

Supplementary Figure 5

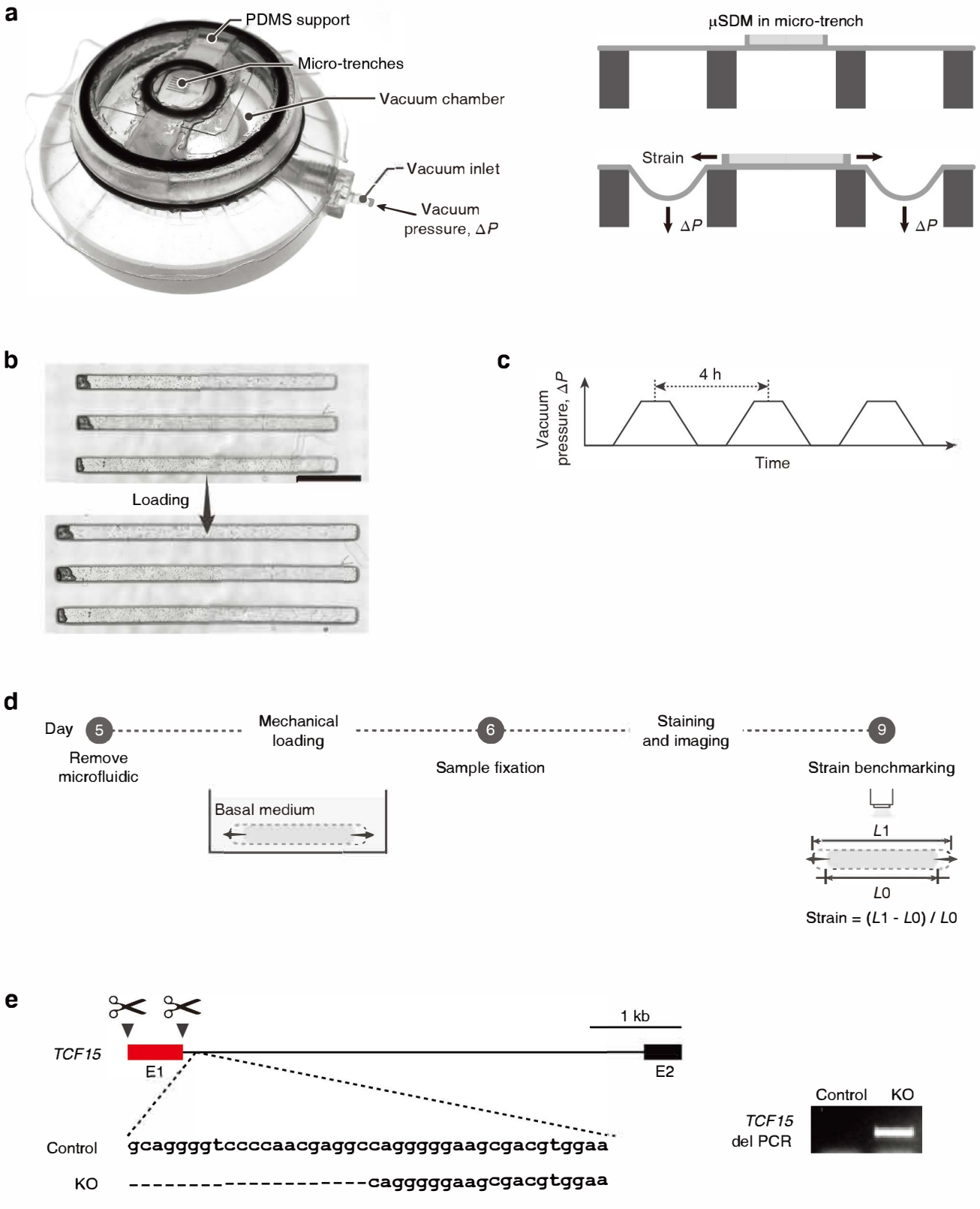

Figure S5. Mechanical stretching of μSDM, related to Figure 5. **a**, (left) Experimental setup of a uniaxial cell stretching device (CSD) with a circular viewing aperture surrounded by a vacuum chamber. Two identical PDMS supports inserted symmetrically in the vacuum chamber divide the chamber into two identical vacuum compartments. (right) A bipolar suction generated by vacuum creates a uniaxial stretching field in the central region of a PDMS basal membrane, on which micro-trenches and μSDM are integrated for dynamic mechanical stretching. Please note that the length of μSDM (the R-C axis) is aligned to be parallel to the uniaxial stretching field. **b**, Brightfield images showing micro-trenches before and under mechanical stretching. Scale bar, 1 mm. **c**, Trapezoidal wave of vacuum pressure with a period of 4 h used for inducing μSDM stretching. **d**, Protocol for μSDM stretching experiments. μSDM tissues are maintained in basal medium and mechanically stretched between Day 5 and 6 for a period of 24 h, before being fixed and stained. After fluorescent imaging, μSDM tissues were stretched again under a brightfield microscope to measure applied strains. **e**, Schematic representation of generation of *TCF15*-KO hESCs using CRISPR/Cas9 genome editing. (left top) Targeted exon 1 (E1) of *TCF15* is shown in red and untargeted exon 2 (E2) is in black. gRNAs are designed to target the promoter region of *TCF15* and downstream intron of exon 1 as indicated. (left bottom) Sequencing results of control and *TCF15*-KO hESCs. (right) PCR validation of gene deletions.

References for Supplementary Information

S1. Zhai, J., Guo, J., Wan, H., Qi, L., Liu, L., Xiao, Z., Yan, L., Schmitz, D.A., Xu, Y., and Yu, D. (2022). Primate gastrulation and early organogenesis at single-cell resolution. Nature, 1-7.

Supplemental Video 1

Click here to access/download

Supplemental Videos and Spreadsheets

Supplementary Video 1.mp4

Supplemental Video 2

Click here to access/download

Supplemental Videos and Spreadsheets

Supplementary Video 2.mp4

Supplemental Video 3

Click here to access/download

Supplemental Videos and Spreadsheets

Supplementary Video 3.mp4

Supplemental Video 4

Click here to access/download

Supplemental Videos and Spreadsheets

Supplementary Video 4.mp4

Supplemental Video 5

Click here to access/download

Supplemental Videos and Spreadsheets

Supplementary Video 5.mp4

CELL PRESS DECLARATION OF INTERESTS POLICY

Transparency is essential for a reader's trust in the scientific process and for the credibility of published articles. At Cell Press, we feel that disclosure of competing interests is a critical aspect of transparency. Therefore, we require a "declaration of interests" section in which all authors disclose any financial or other interests related to the submitted work that (1) could affect or have the perception of affecting the author's objectivity or (2) could influence or have the perception of influencing the content of the article.

What types of articles does this apply to?

We require that you disclose competing interests for all submitted content by completing and submitting the form below. We also require that you include a "declaration of interests" section in the text of all articles even if there are no interests to declare.

What should I disclose?

We require that you and all authors disclose any personal financial interests (e.g., stocks or shares in companies with interests related to the submitted work or consulting fees from companies that could have interests related to the work), professional affiliations, advisory positions, board memberships (including membership on a journal's advisory board when publishing in that journal), or patent holdings that are related to the subject matter of the contribution. As a guideline, you need to declare an interest for (1) any affiliation associated with a payment or financial benefit exceeding $10,000 p.a. or 5% ownership of a company or (2) research funding by a company with related interests. You do not need to disclose diversified mutual funds, 401ks, or investment trusts.

Authors should also disclose relevant financial interests of immediate family members. Cell Press uses the Public Health Service definition of "immediate family member," which includes spouse and dependent children.

Where do I declare competing interests?

Competing interests should be disclosed on this form as well as in a "declaration of interests" section in the manuscript. This section should include financial or other competing interests as well as affiliations that are not included in the author list. Examples of "declaration of interests" language include:

> "AUTHOR is an employee and shareholder of COMPANY."
> "AUTHOR is a founder of COMPANY and a member of its scientific advisory board."

NOTE: Primary affiliations should be included with the author list and do not need to be included in the "declaration of interests" section. Funding sources should be included in the "acknowledgments" section and also do not need to be included in the "declaration of interests" section. (A small number of front-matter article types do not include an "acknowledgments" section. For these articles, reporting of funding sources is not required.)

What if there are no competing interests to declare?

If you have no competing interests to declare, please note that in the "declaration of interests" section with the following wording:

> "The authors declare no competing interests."

CELL PRESS DECLARATION OF INTERESTS FORM

If submitting materials via Editorial Manager, please complete this form and upload with your initial submission. Otherwise, please email as an attachment to the editor handling your manuscript.

Please complete each section of the form and insert any necessary "declaration of interests" statement in the text box at the end of the form. A matching statement should be included in a "declaration of interests" section in the manuscript.

Institutional affiliations

We require that you list the current institutional affiliations of all authors, including academic, corporate, and industrial, on the title page of the manuscript. ***Please select one of the following:***

☒ All affiliations are listed on the title page of the manuscript.

☐ I or other authors have additional affiliations that we have noted in the "declaration of interests" section of the manuscript and on this form below.

Funding sources

We require that you disclose all funding sources for the research described in this work. ***Please confirm the following:***

☒ All funding sources for this study are listed in the "acknowledgments" section of the manuscript.*

*A small number of front-matter article types do not include an "acknowledgments" section. For these, reporting funding sources is not required.

Competing financial interests

We require that authors disclose any financial interests and any such interests of immediate family members, including financial holdings, professional affiliations, advisory positions, board memberships, receipt of consulting fees, etc., that:

(1) could affect or have the perception of affecting the author's objectivity, *or*
(2) could influence or have the perception of influencing the content of the article.

Please select one of the following:

☒ We, the authors and our immediate family members, have no financial interests to declare.

☐ We, the authors, have noted any financial interests in the "declaration of interests" section of the manuscript and on this form below, and we have noted interests of our immediate family members.

Advisory/management and consulting positions

We require that authors disclose any position, be it a member of a board or advisory committee or a paid consultant, that they have been involved with that is related to this study. We also require that members of our journal advisory boards disclose their position when publishing in that journal. ***Please select one of the following:***

☒ We, the authors and our immediate family members, have no positions to declare and are not members of the journal's advisory board.

☐ The authors and/or their immediate family members have management/advisory or consulting relationships noted in the "declaration of interests" section of the manuscript and on this form below.

Patents

We require that you disclose any patents related to this work by any of the authors or their institutions. ***Please select one of the following:***

☒ We, the authors and our immediate family members, have no related patents to declare.

☐ We, the authors, have a patent related to this work, which is noted in the "declaration of interests" section of the manuscript and on this form below, and we have noted the patents of immediate family members.

Please insert any "declaration of interests" statements in this space. This exact text should also be included in the "declaration of interests" section of the manuscript. If no authors have a competing interest, please insert the text, "The authors declare no competing interests."

The authors declare no competing interests.

☒ **On behalf of all authors, I declare that I have disclosed all competing interests related to this work. If any exist, they have been included in the "declaration of interests" section of the manuscript.**